International Journal of Numerical Methods for He
Flui

A novel finite-element-based solution and property construction method for thermal problems from sparse data

Journal:	*International Journal of Numerical Methods for Heat and Fluid Flow*
Manuscript ID	HFF-03-2025-0209.R2
Manuscript Type:	Research Article
Keywords:	Solution construction, Material properties, Sparse data, Finite element method, ODIL concept, Nuclear fusion

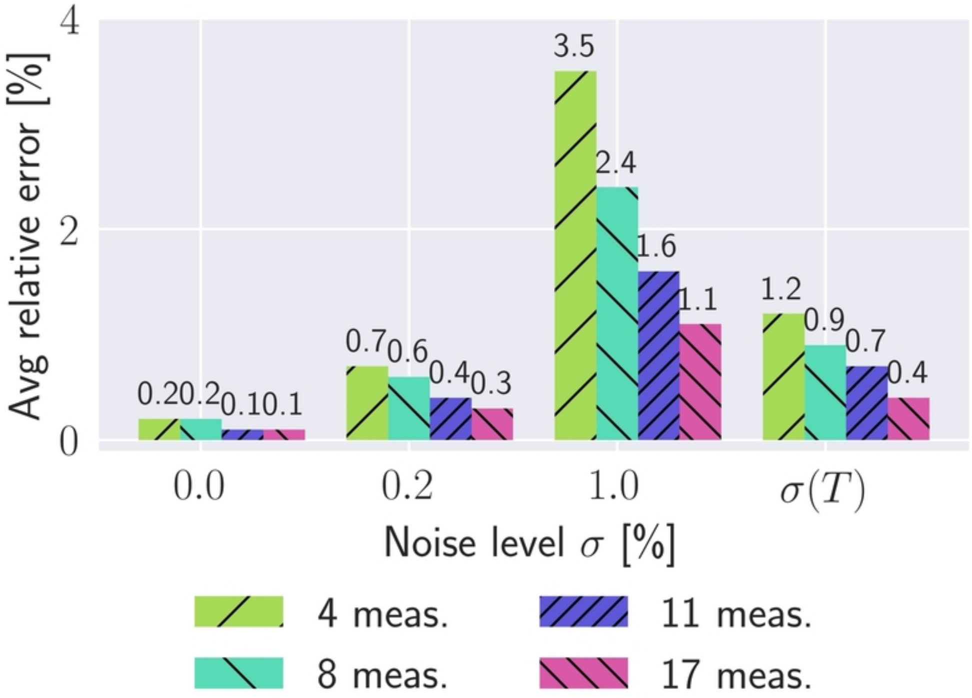

135x101mm (150 x 150 DPI)

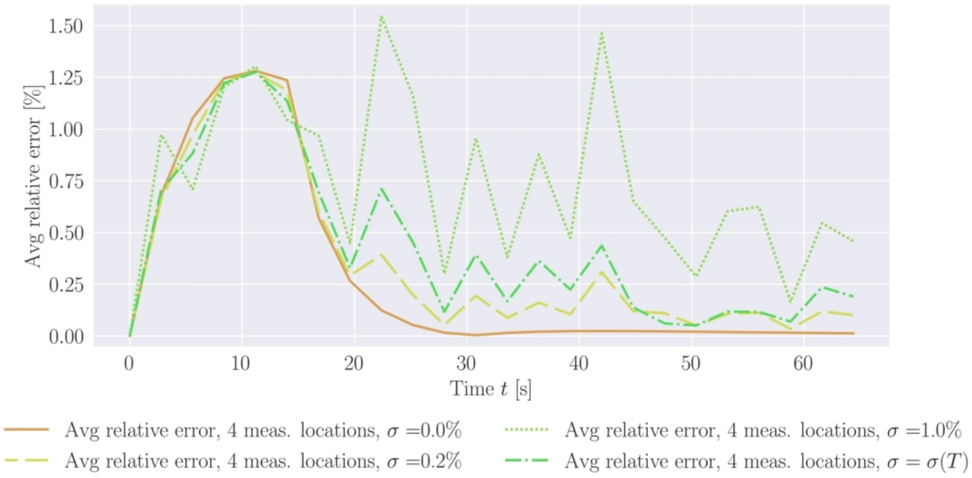

280x138mm (150 x 150 DPI)

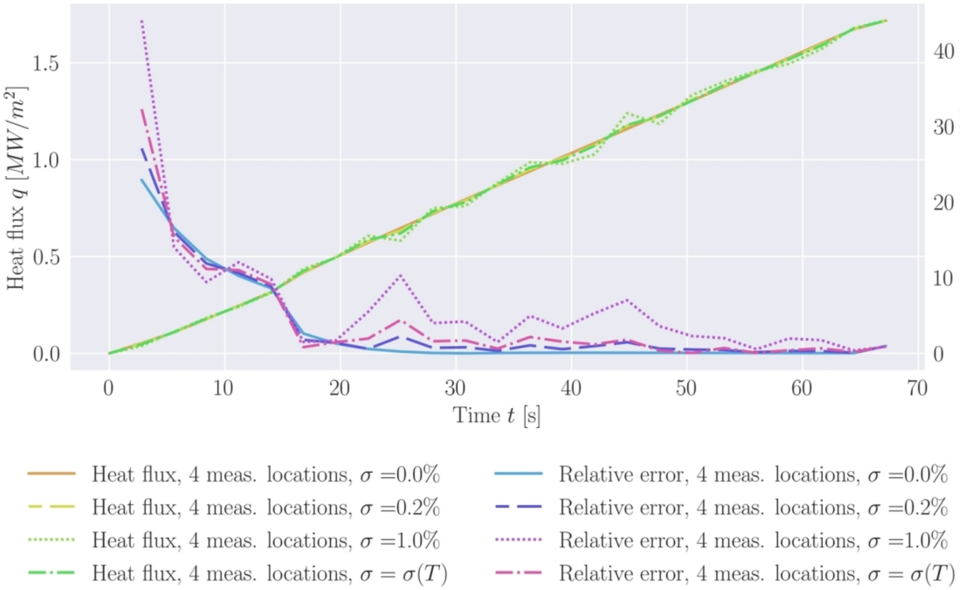

261x159mm (150 x 150 DPI)

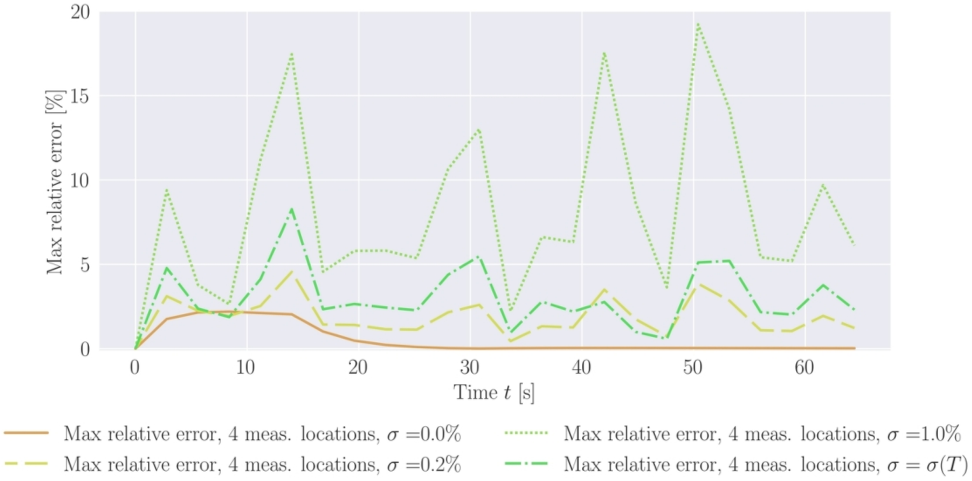

282x140mm (150 x 150 DPI)

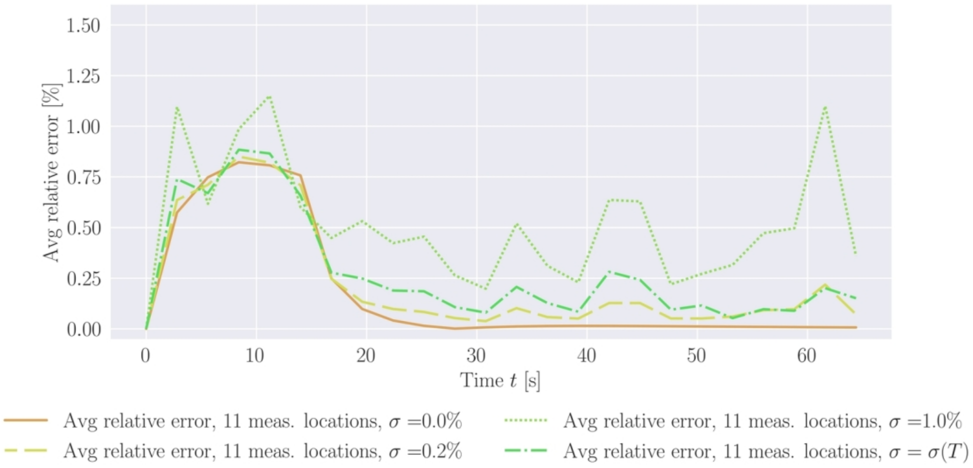

286x138mm (150 x 150 DPI)

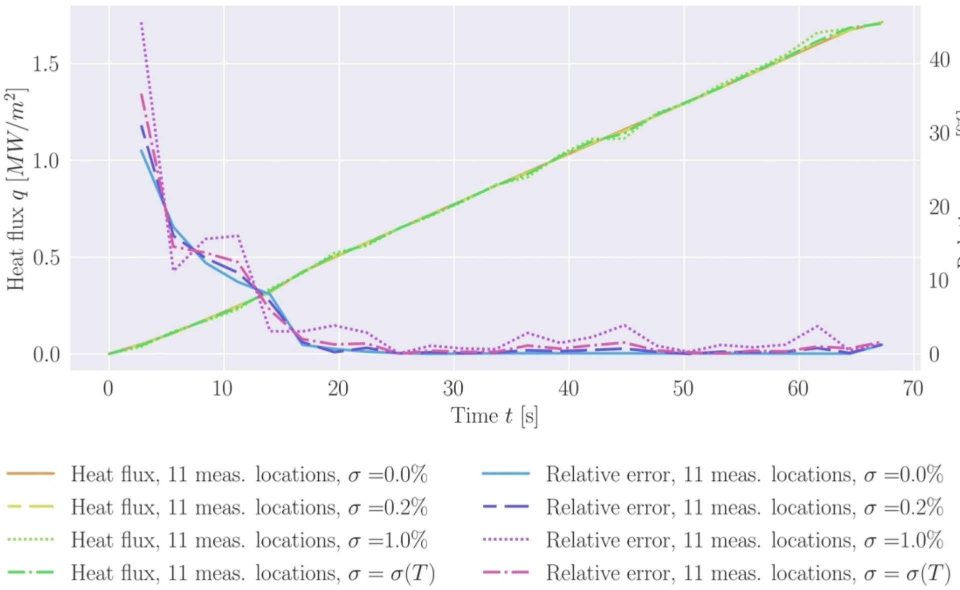

262x159mm (150 x 150 DPI)

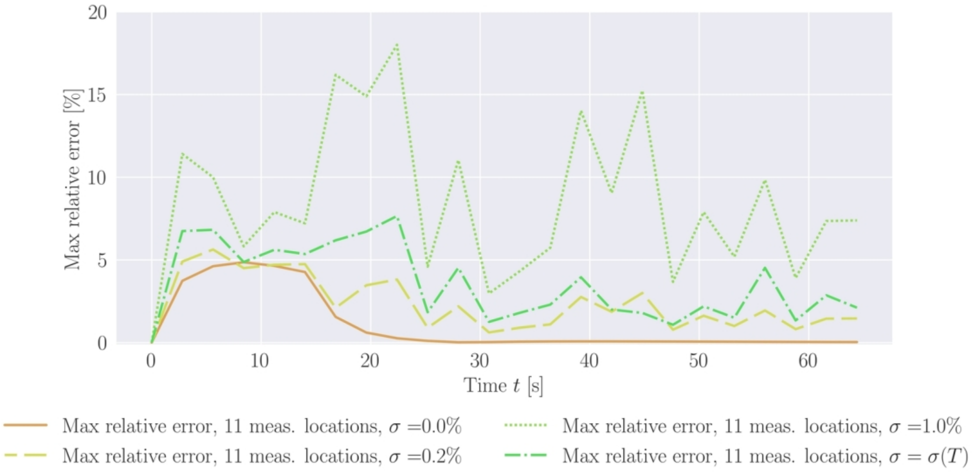

287x140mm (150 x 150 DPI)

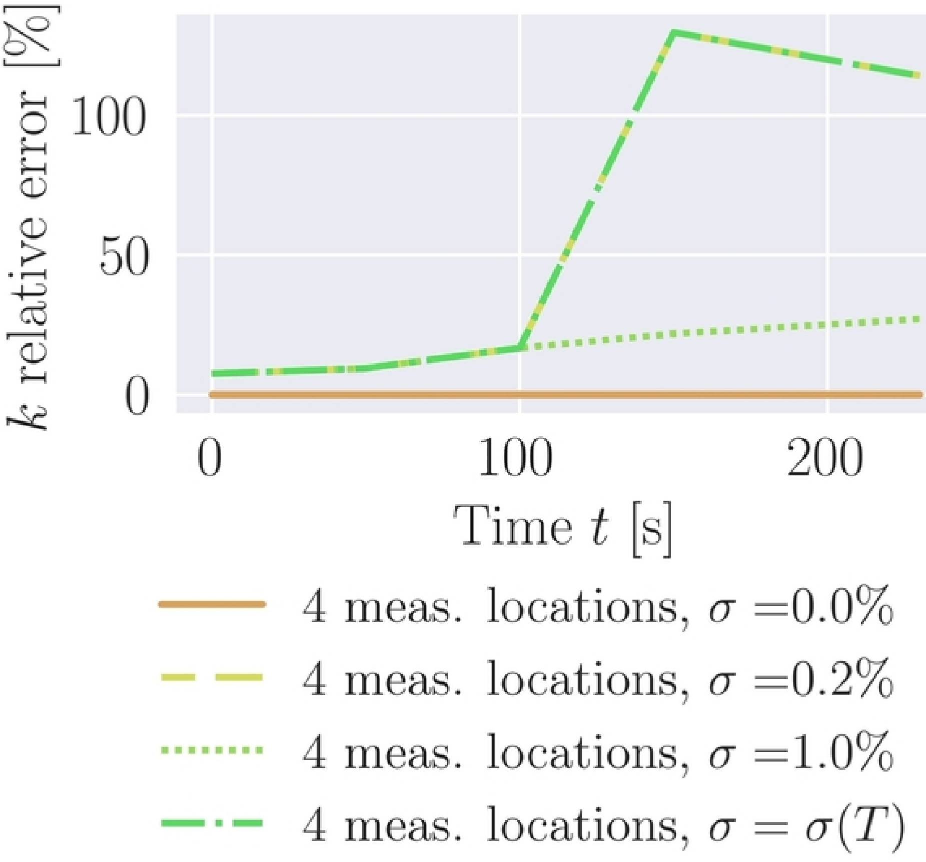

104x94mm (150 x 150 DPI)

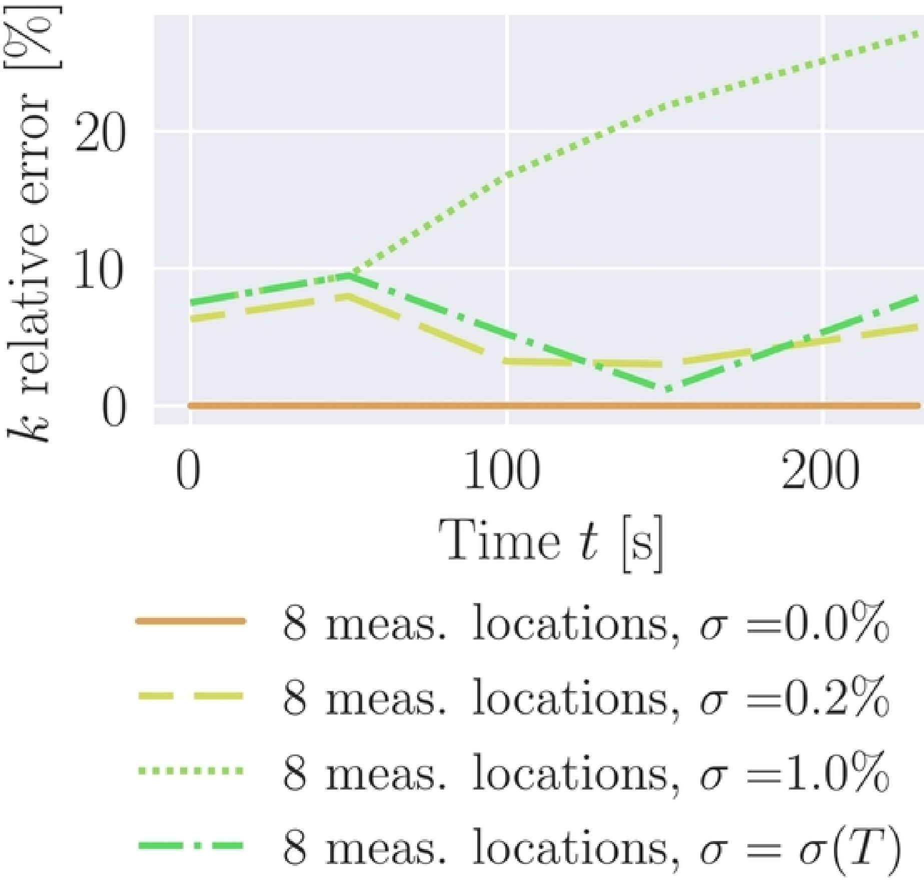

101x94mm (150 x 150 DPI)

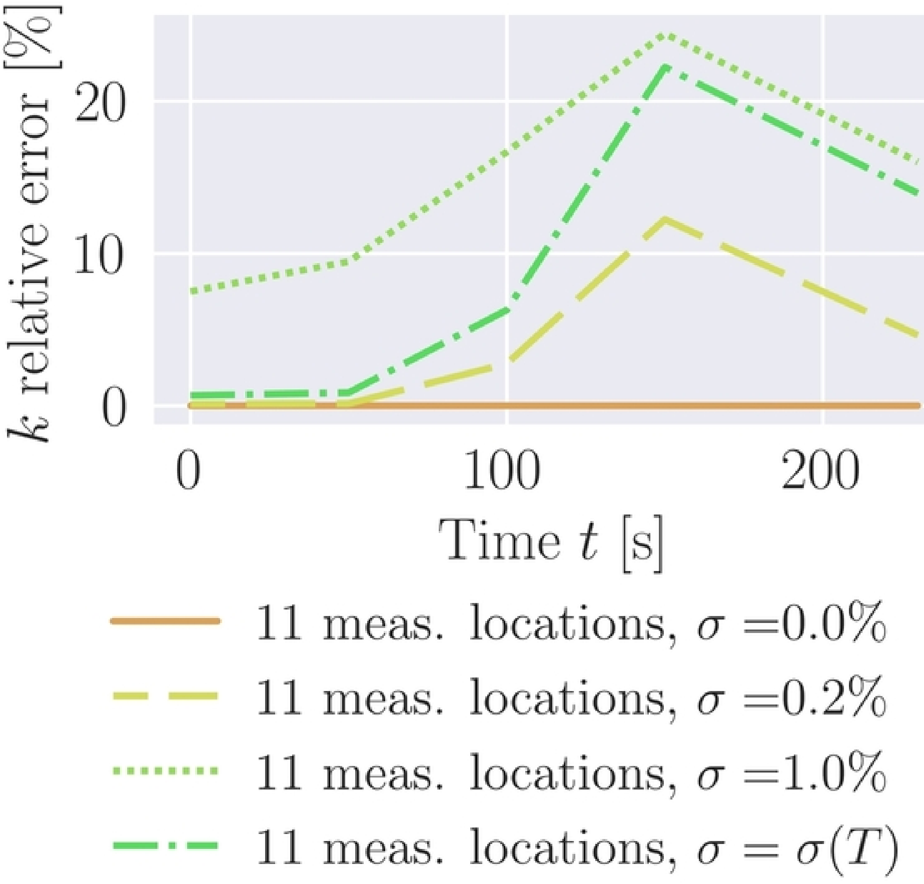

101x94mm (150 x 150 DPI)

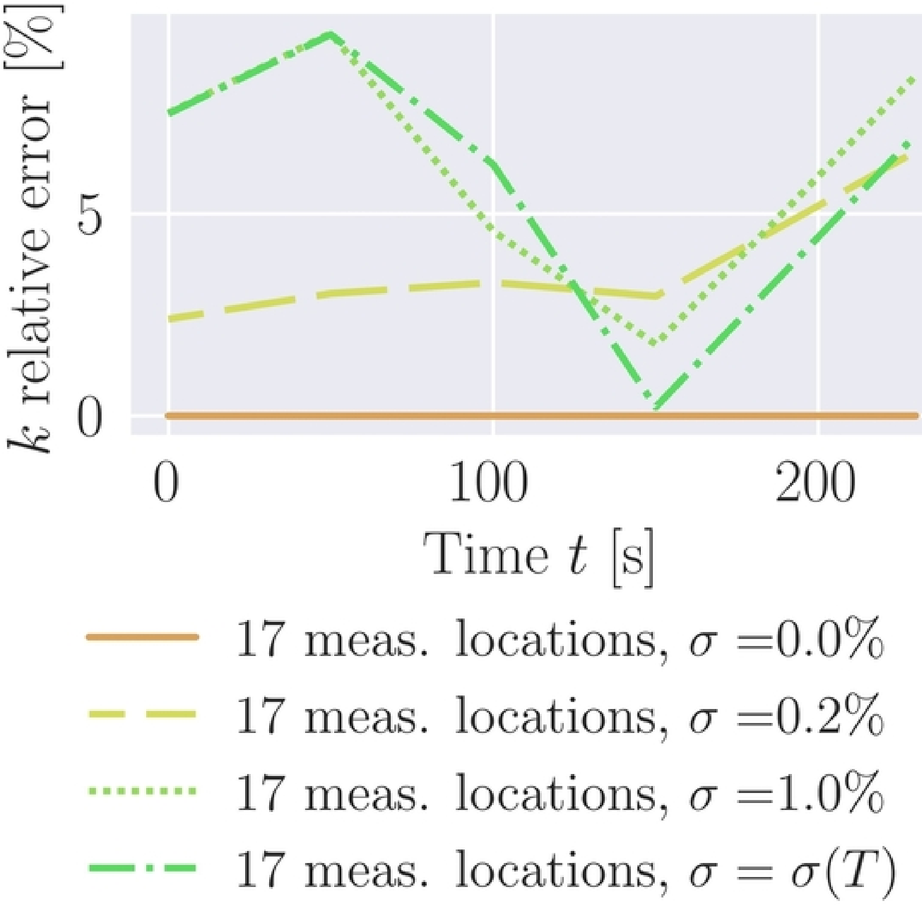

98x94mm (150 x 150 DPI)

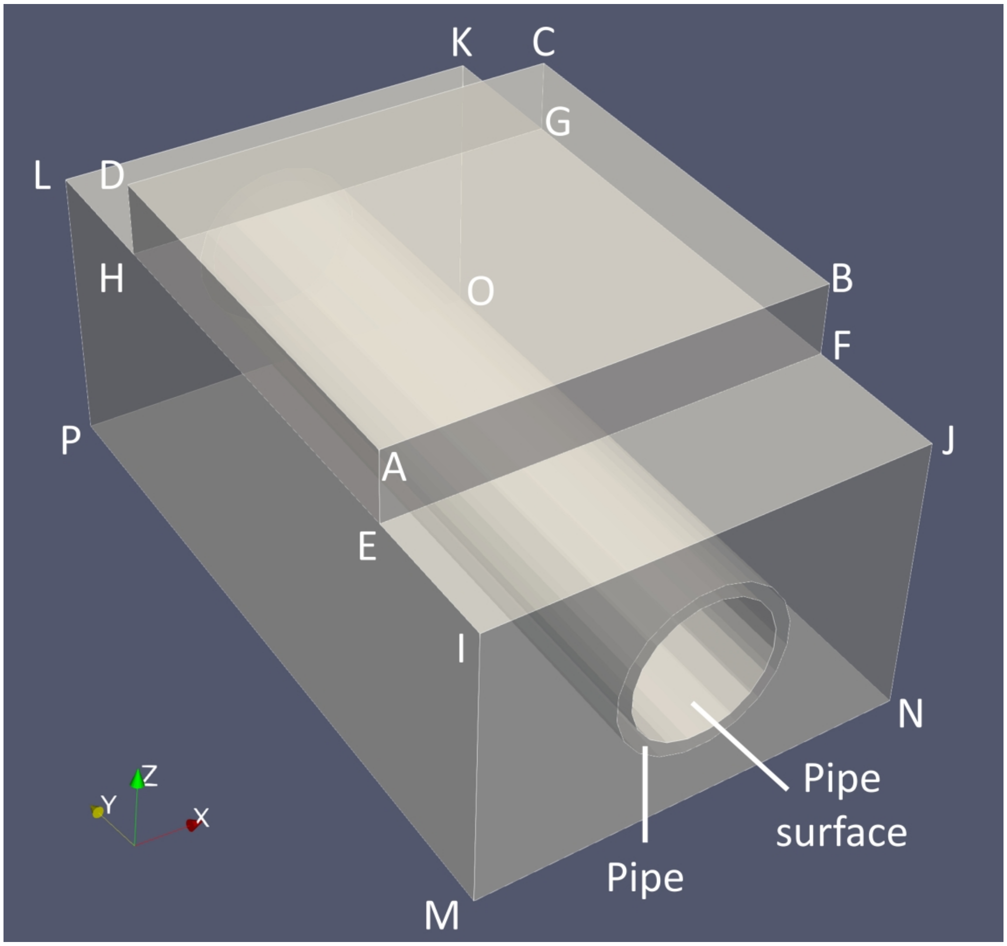

515x482mm (150 x 150 DPI)

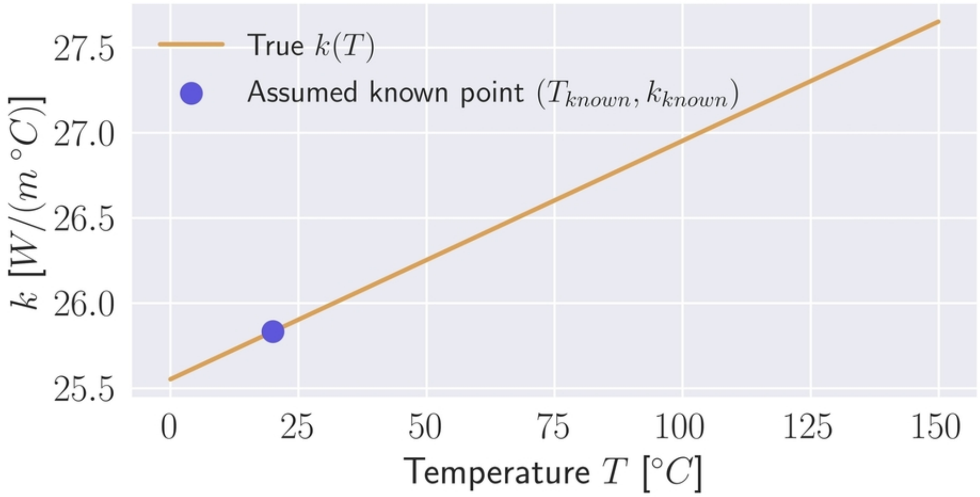

158x82mm (150 x 150 DPI)

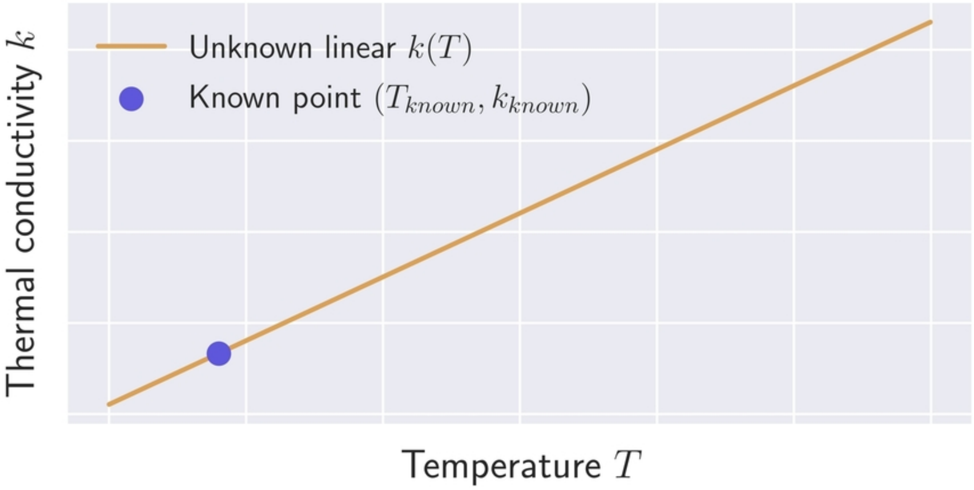

148x76mm (150 x 150 DPI)

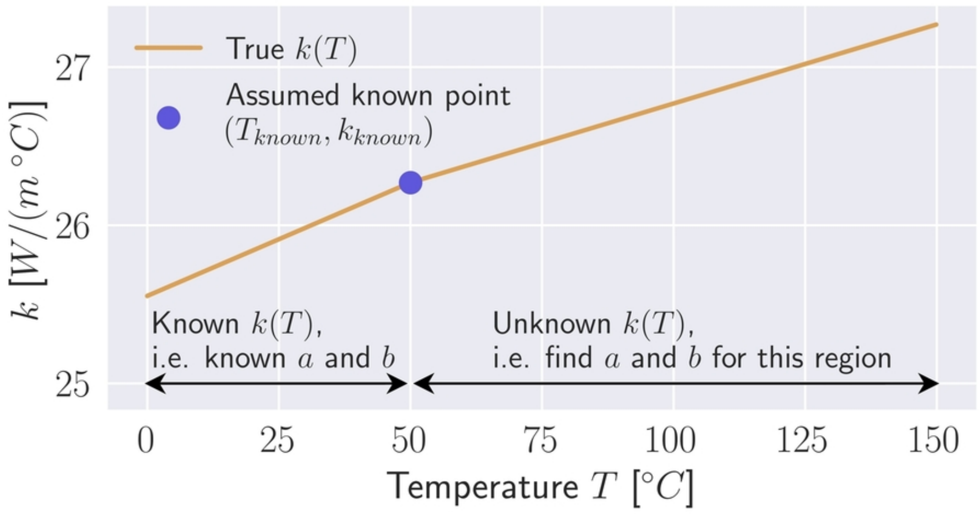

154x82mm (150 x 150 DPI)

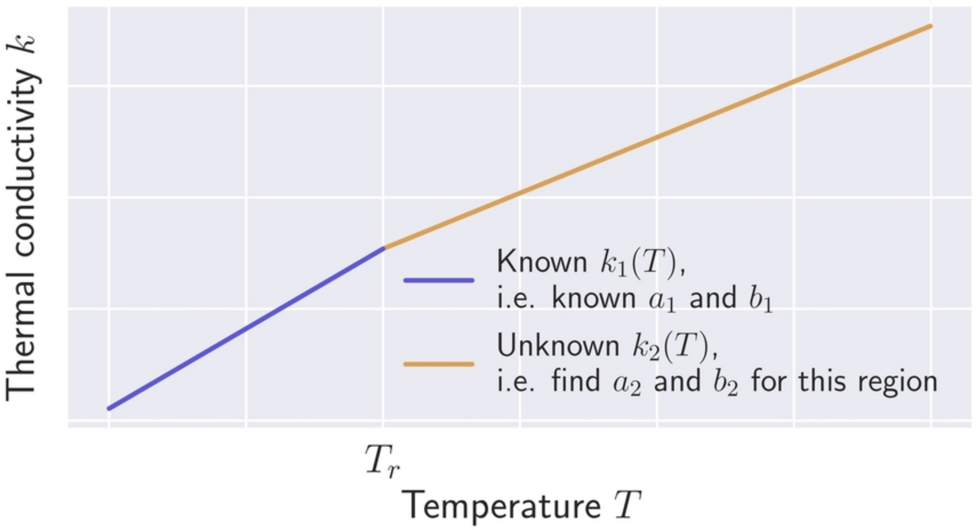

148x81mm (150 x 150 DPI)

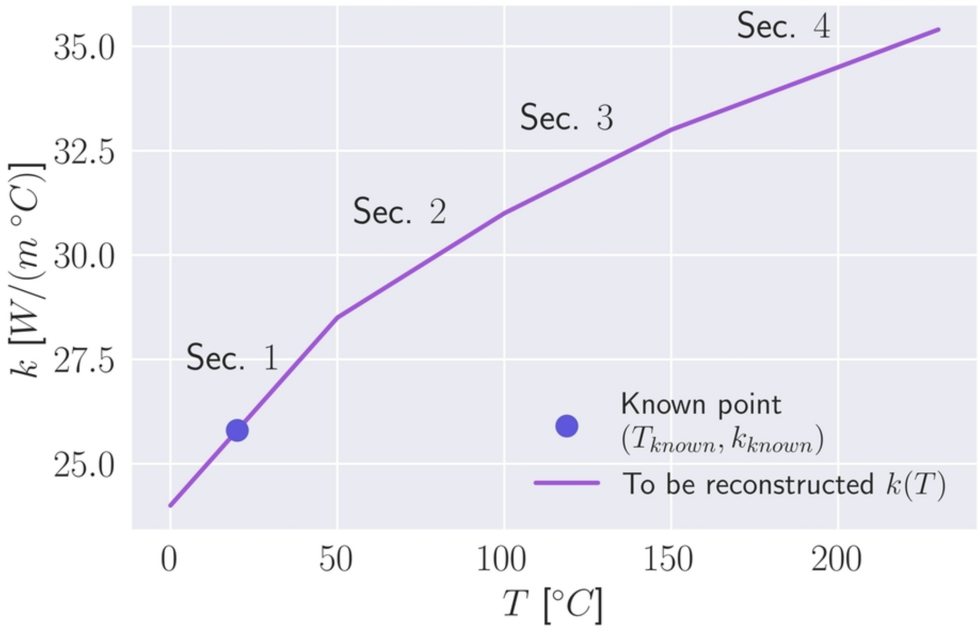

158x103mm (150 x 150 DPI)

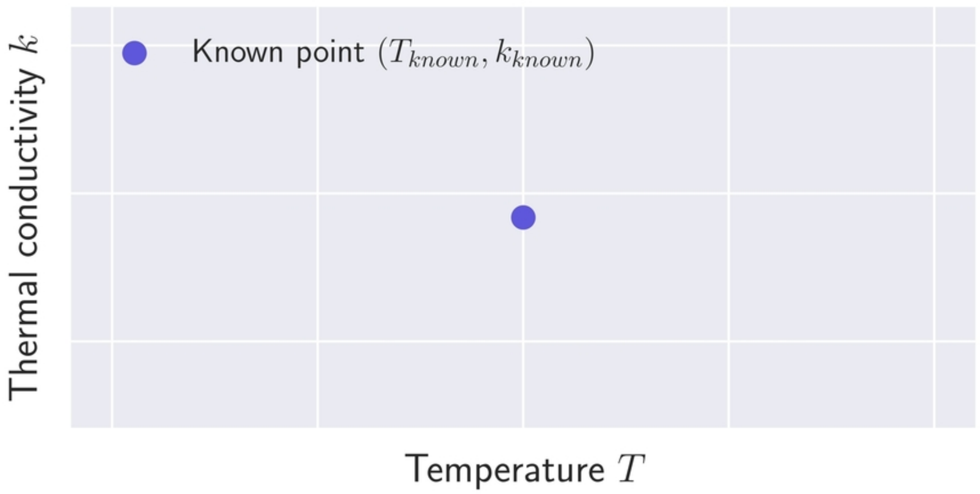

148x76mm (150 x 150 DPI)

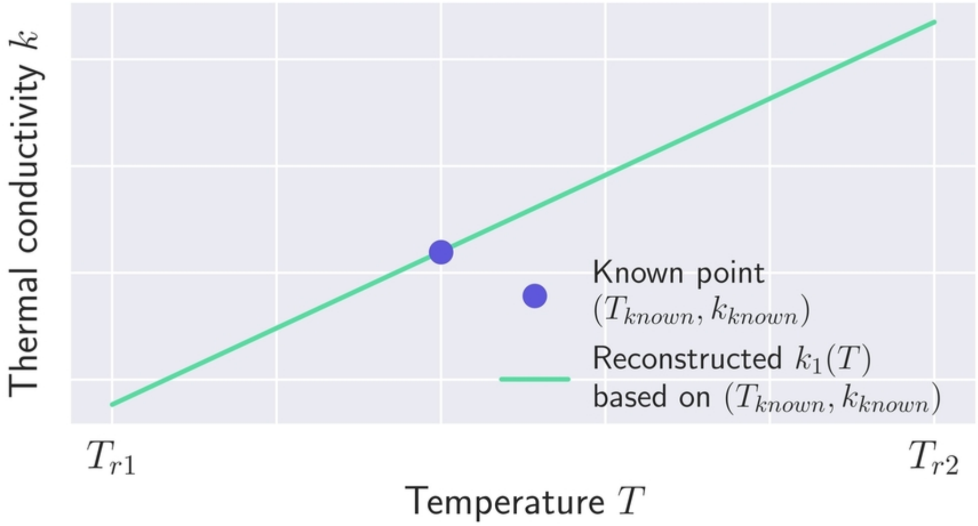

148x81mm (150 x 150 DPI)

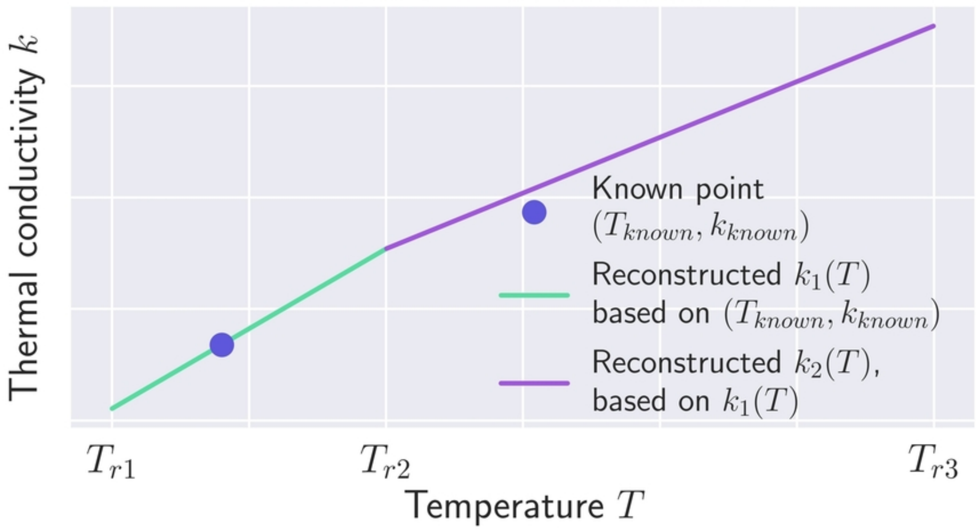

148x81mm (150 x 150 DPI)

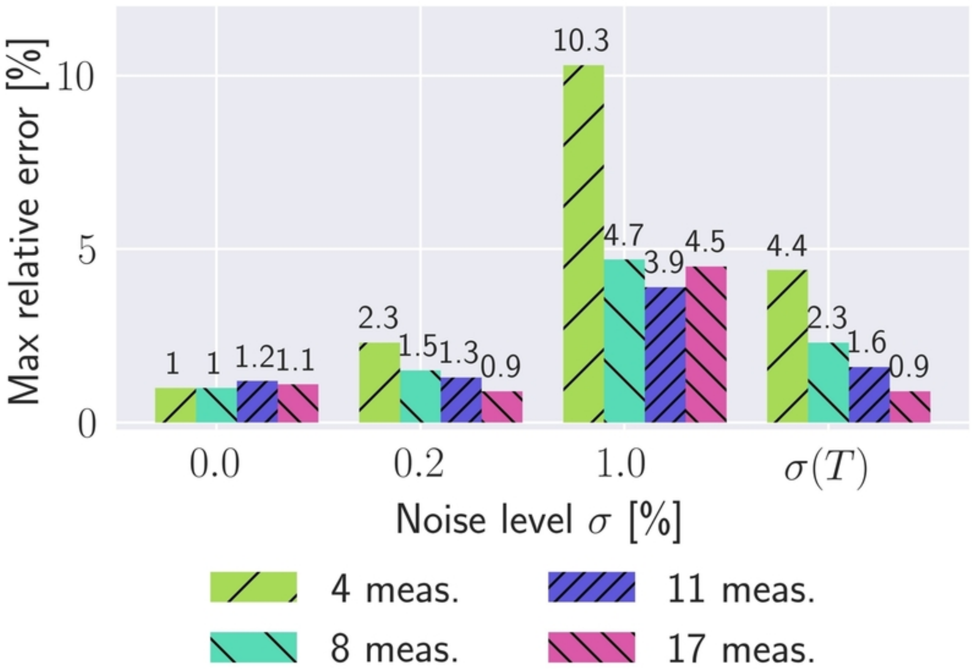

138x99mm (150 x 150 DPI)

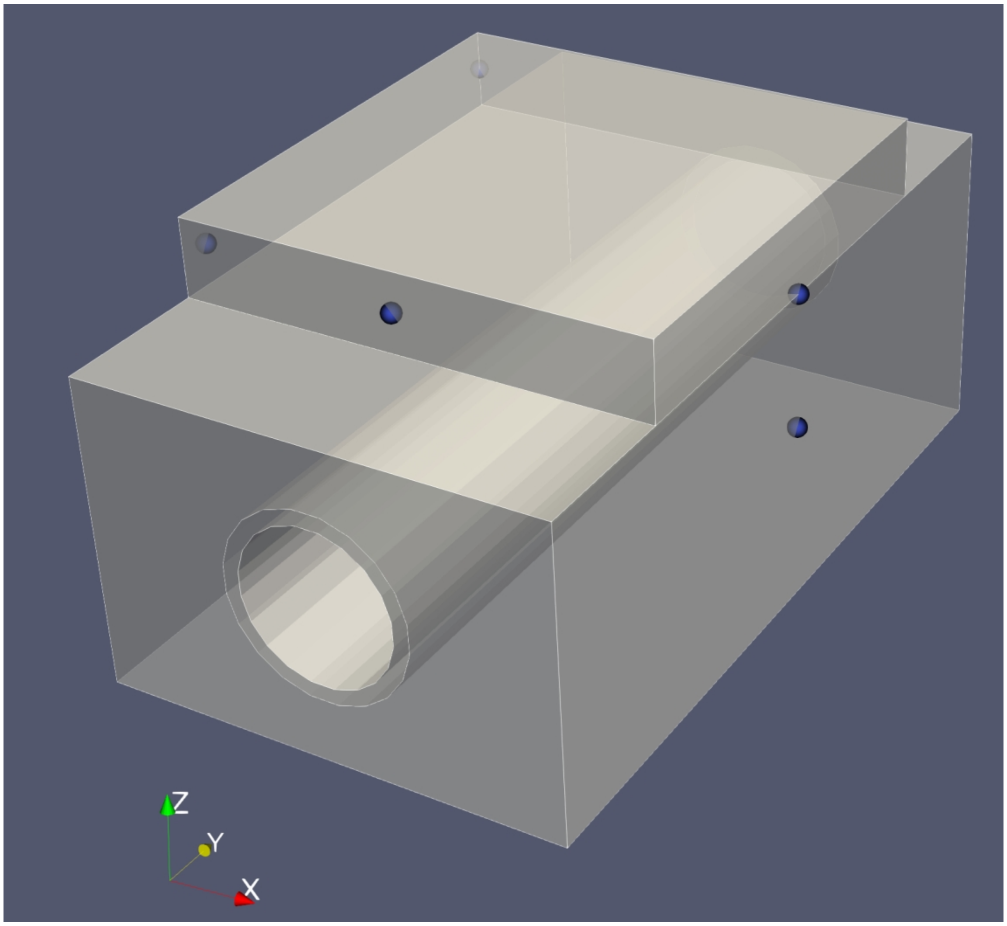

1155x1060mm (38 x 38 DPI)

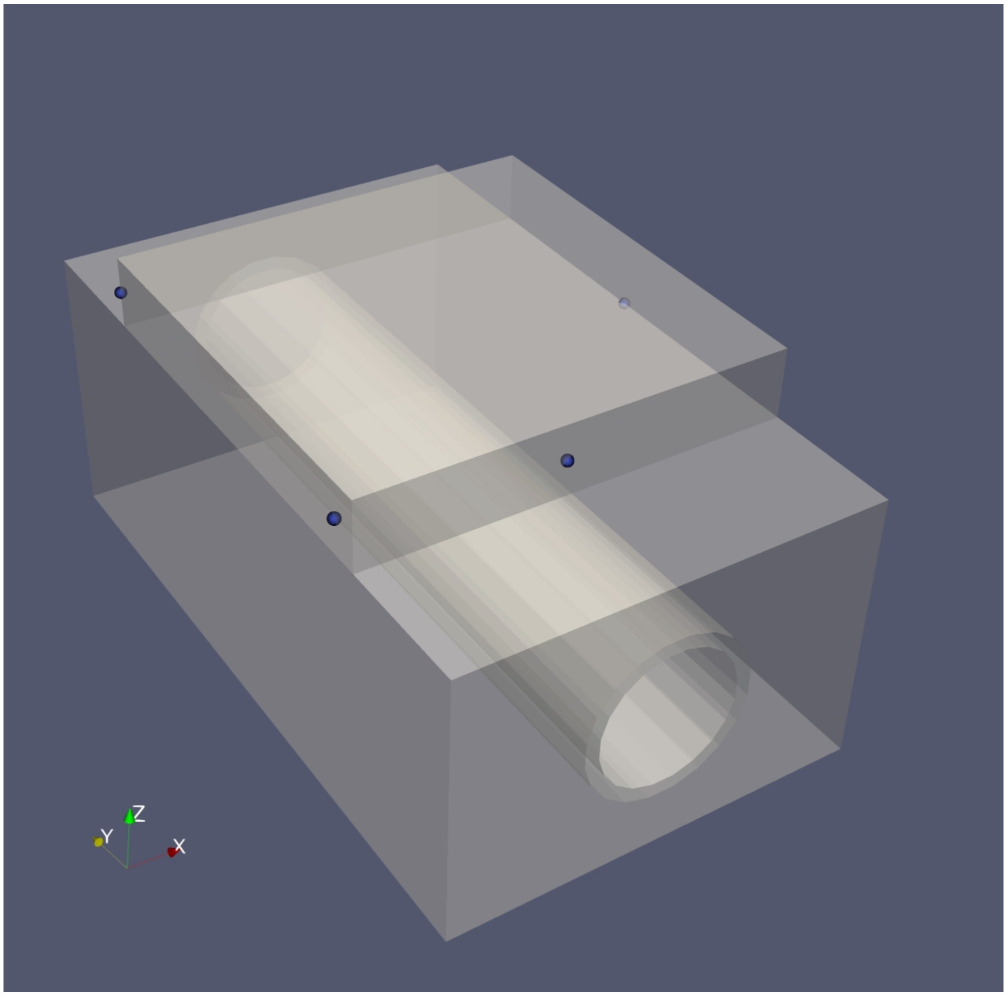

1554x1536mm (38 x 38 DPI)

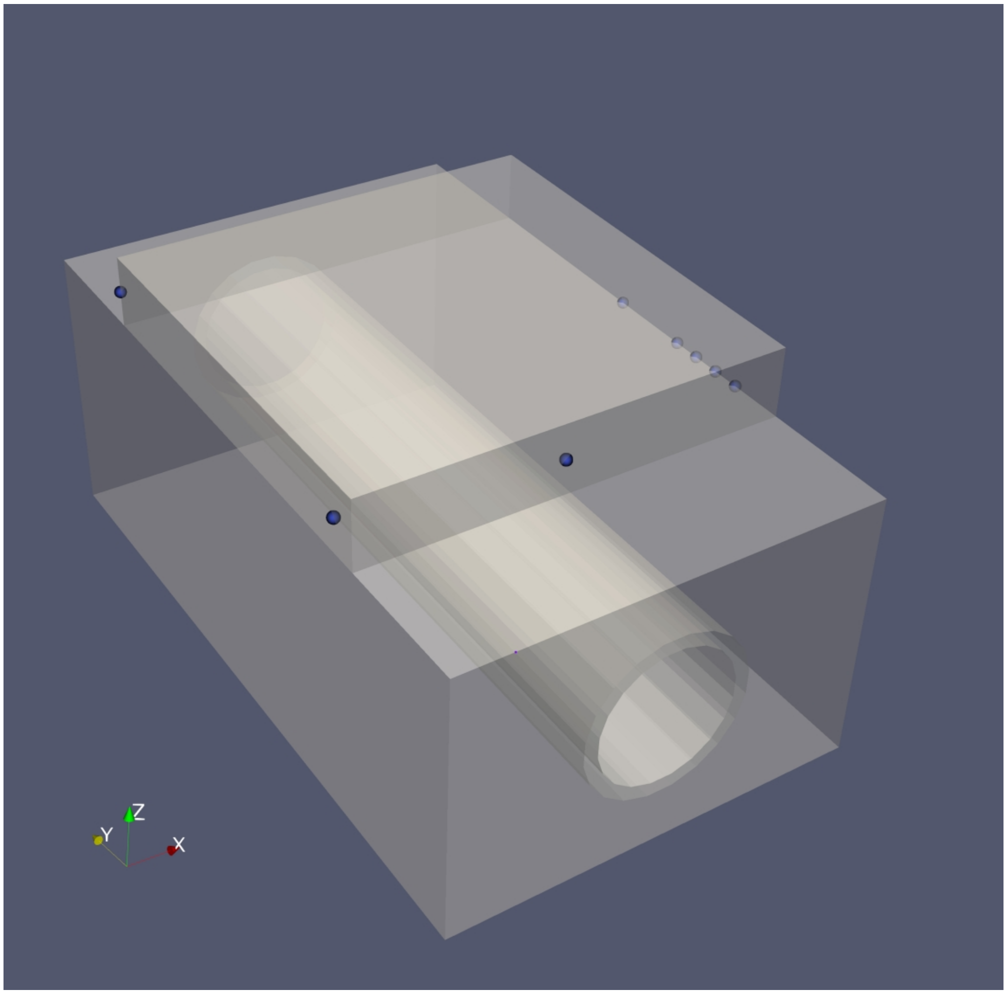

1557x1536mm (38 x 38 DPI)

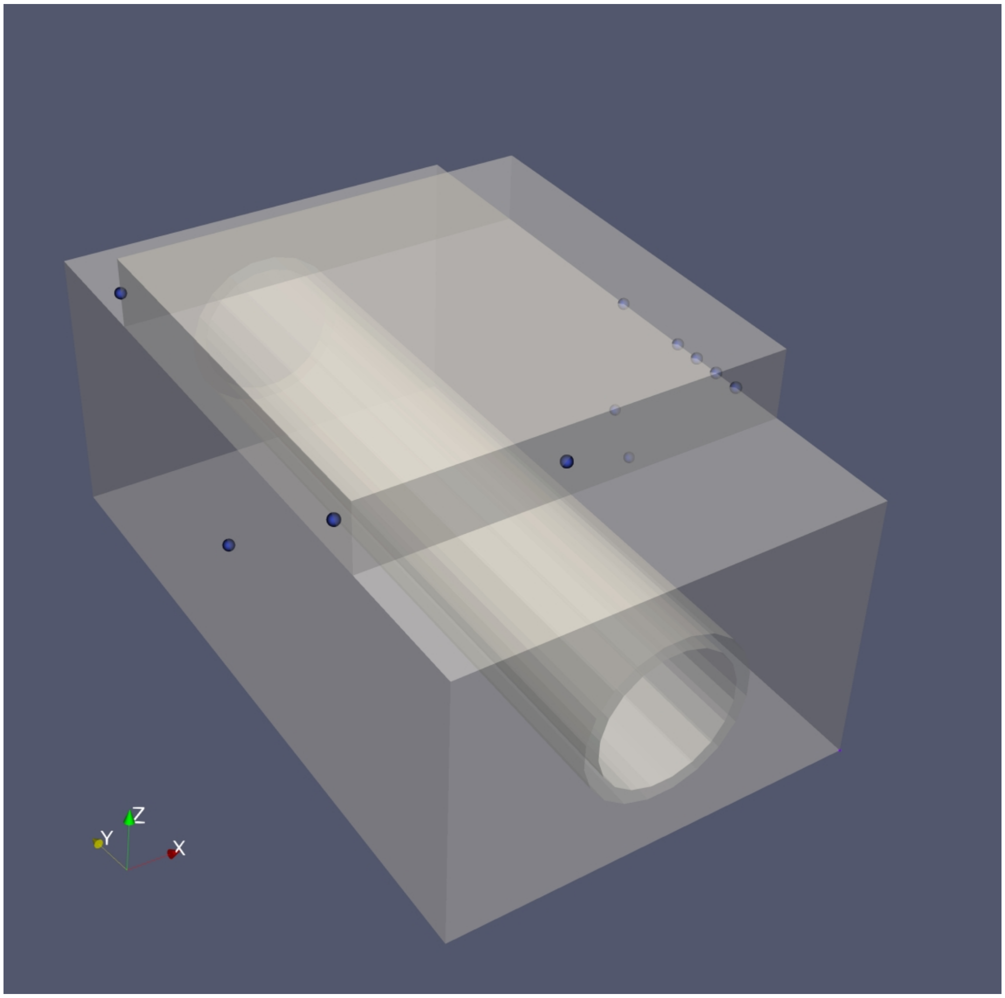

1552x1536mm (38 x 38 DPI)

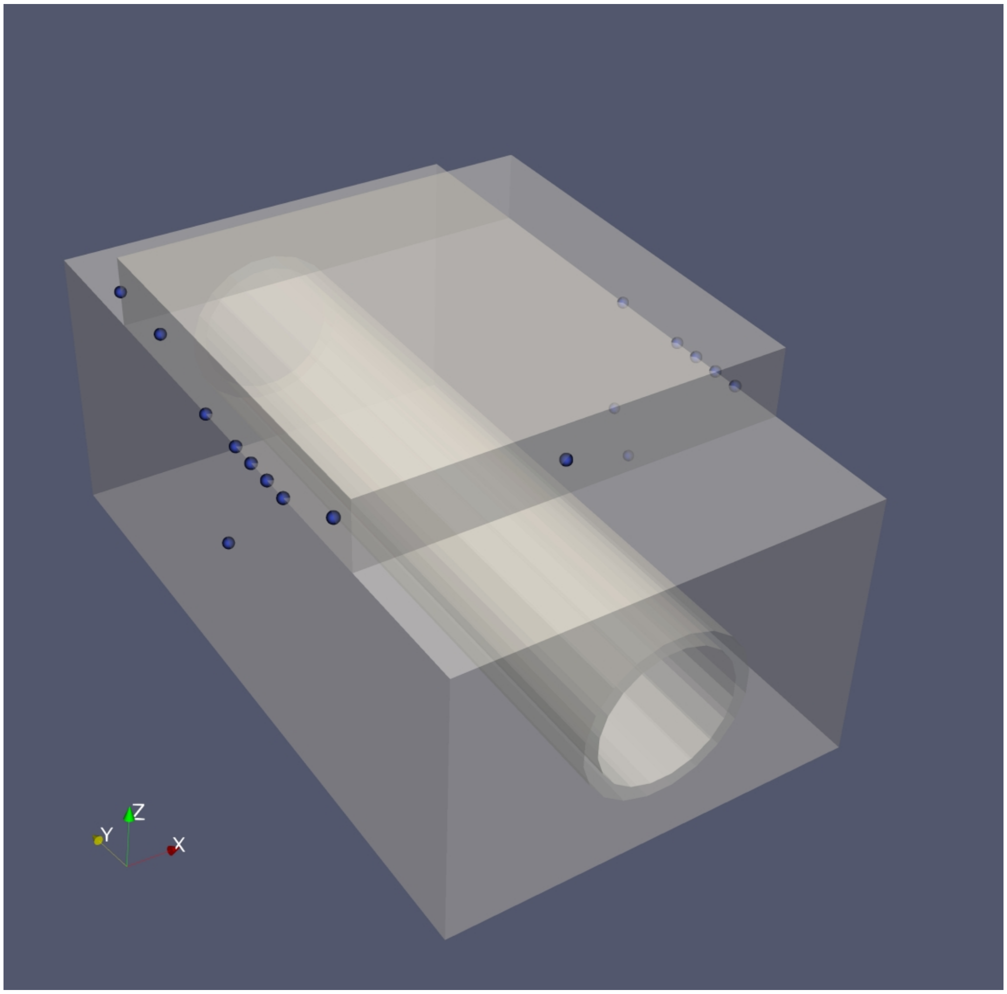

1557x1536mm (38 x 38 DPI)

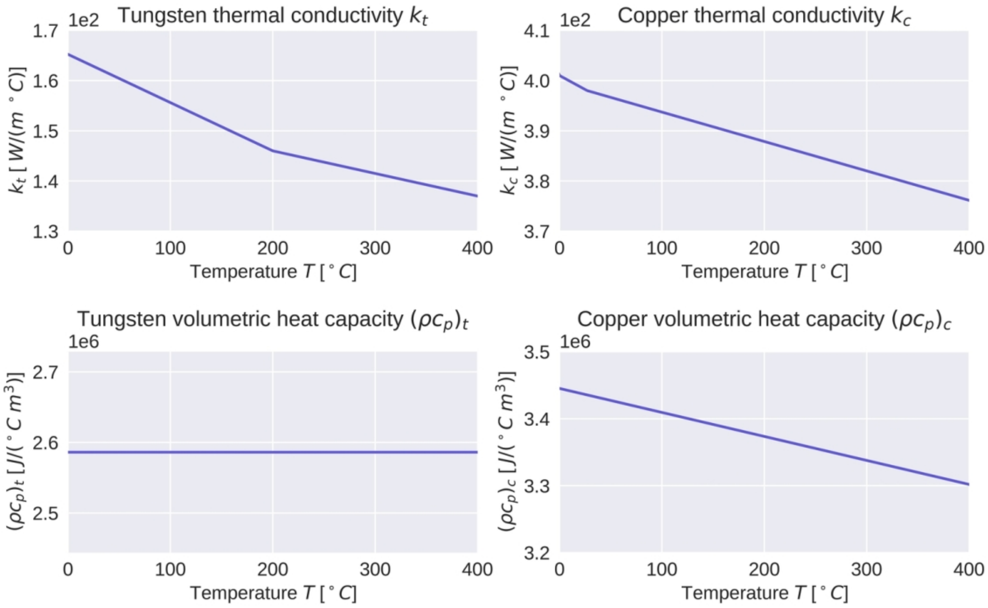

262x161mm (150 x 150 DPI)

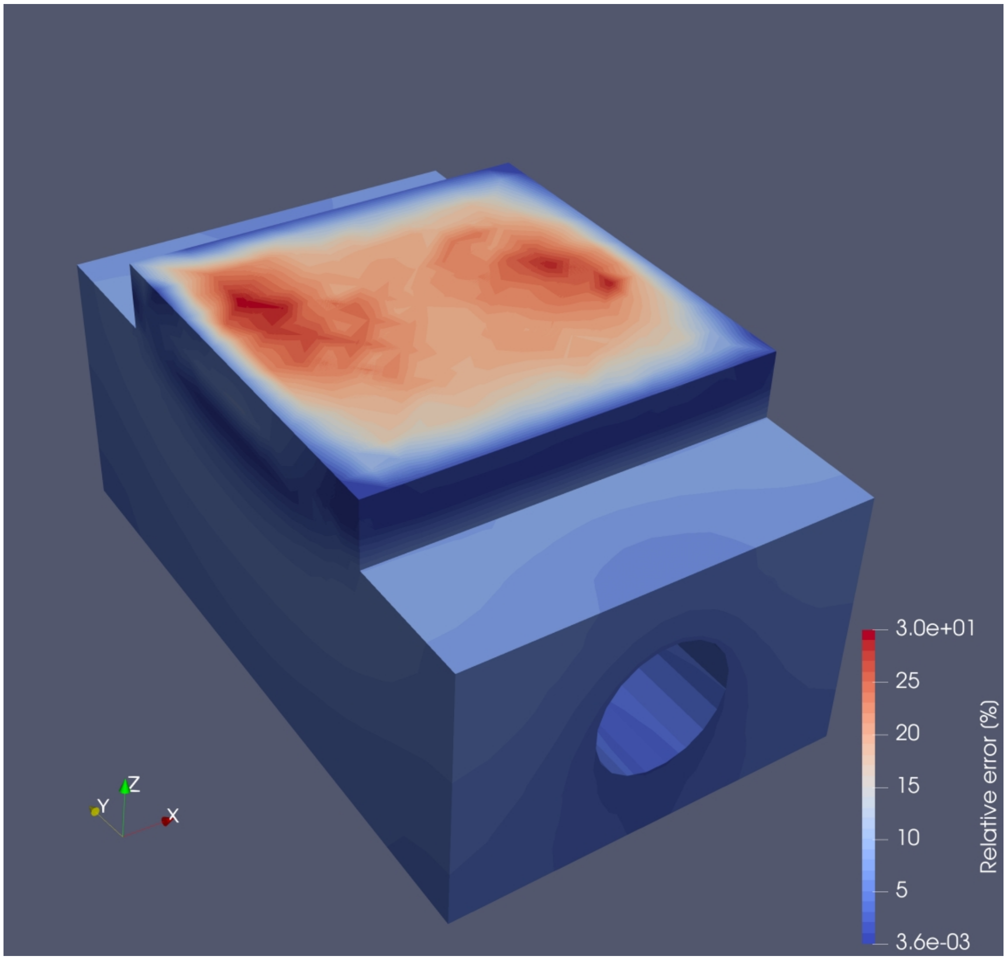

850x810mm (72 x 72 DPI)

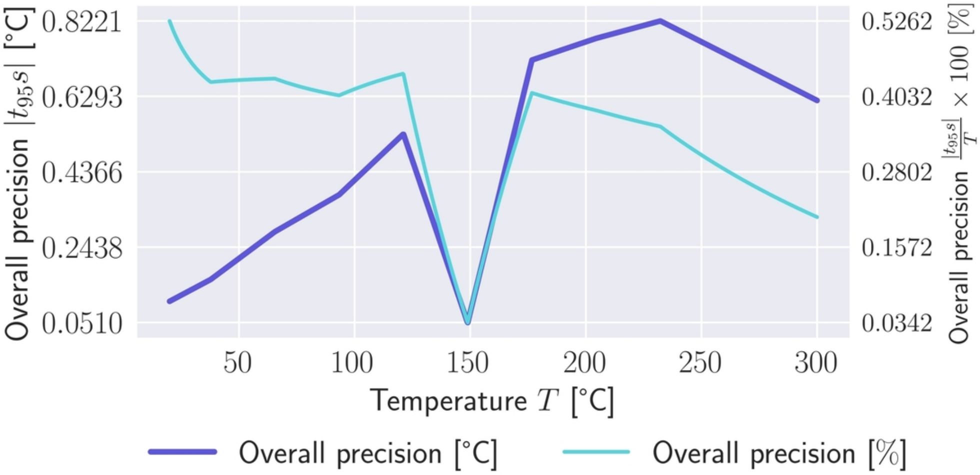

188x94mm (150 x 150 DPI)

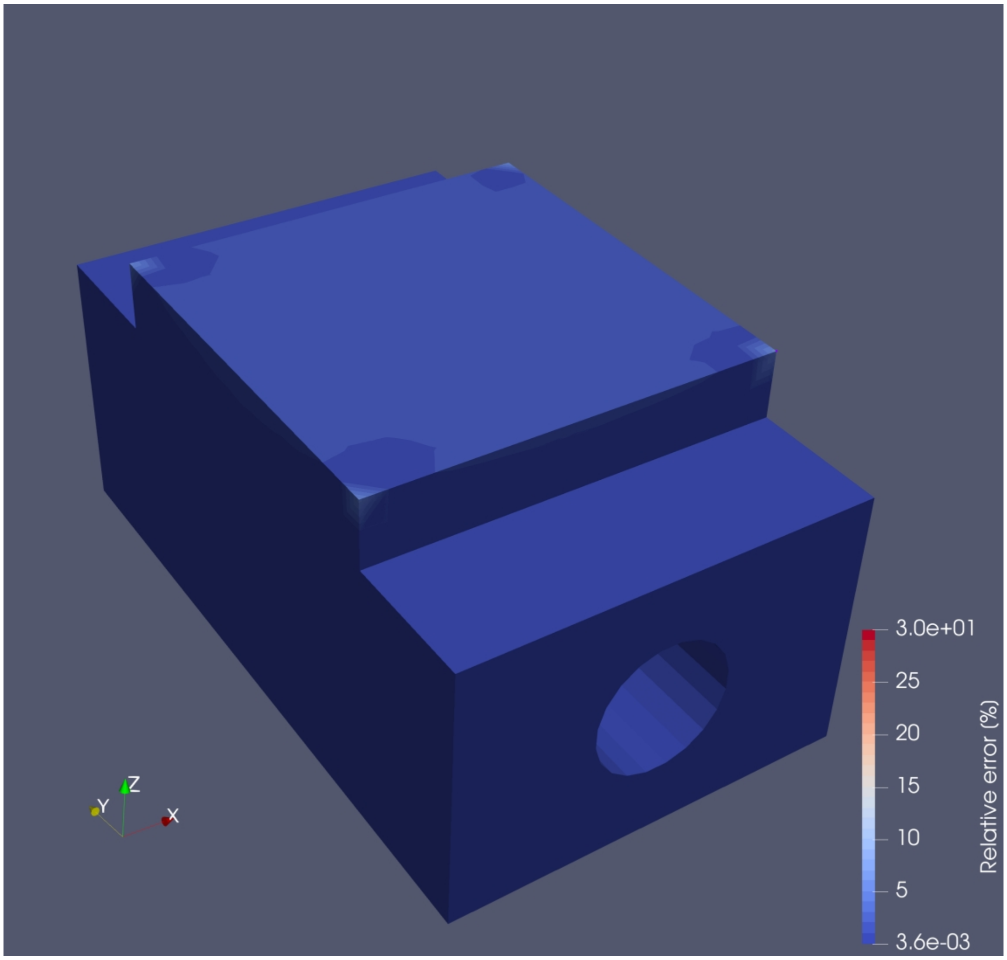

850x810mm (72 x 72 DPI)

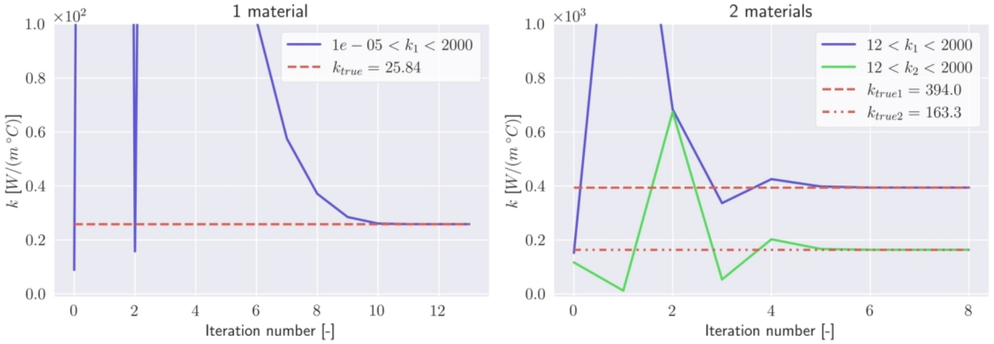

304x107mm (150 x 150 DPI)

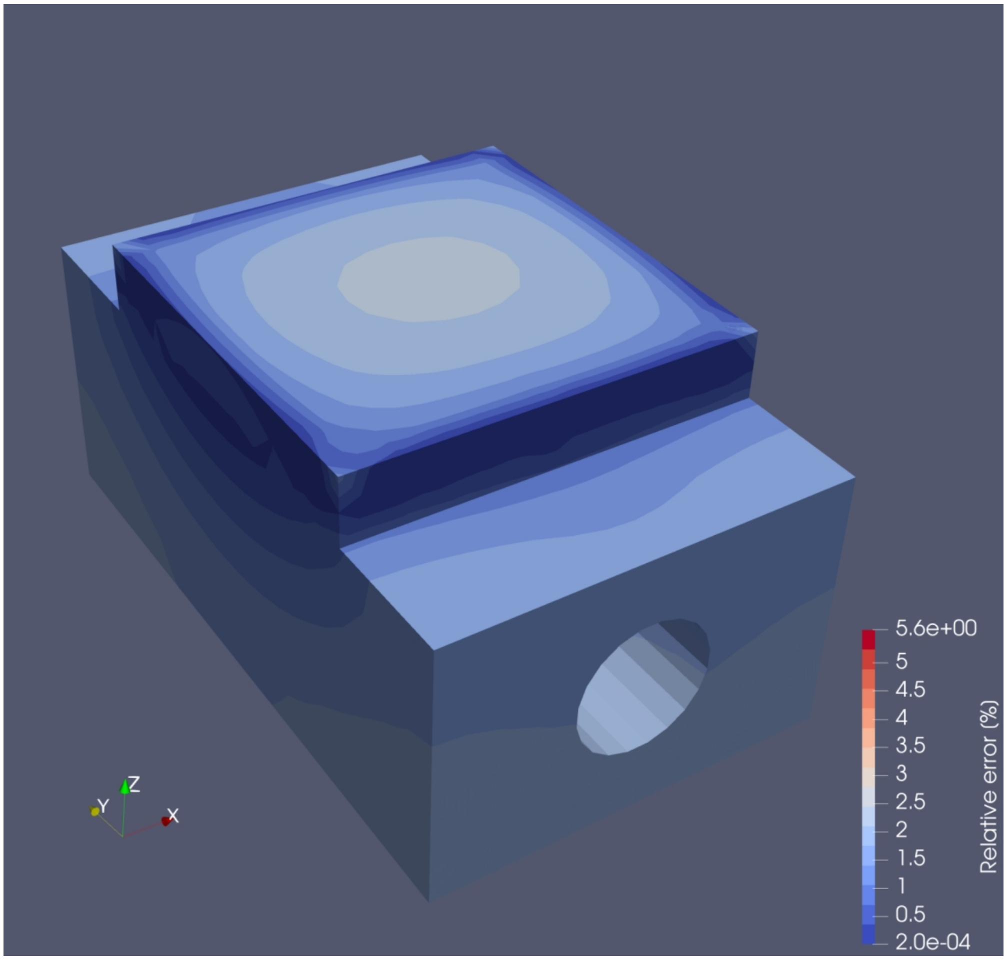

1531x1458mm (28 x 28 DPI)

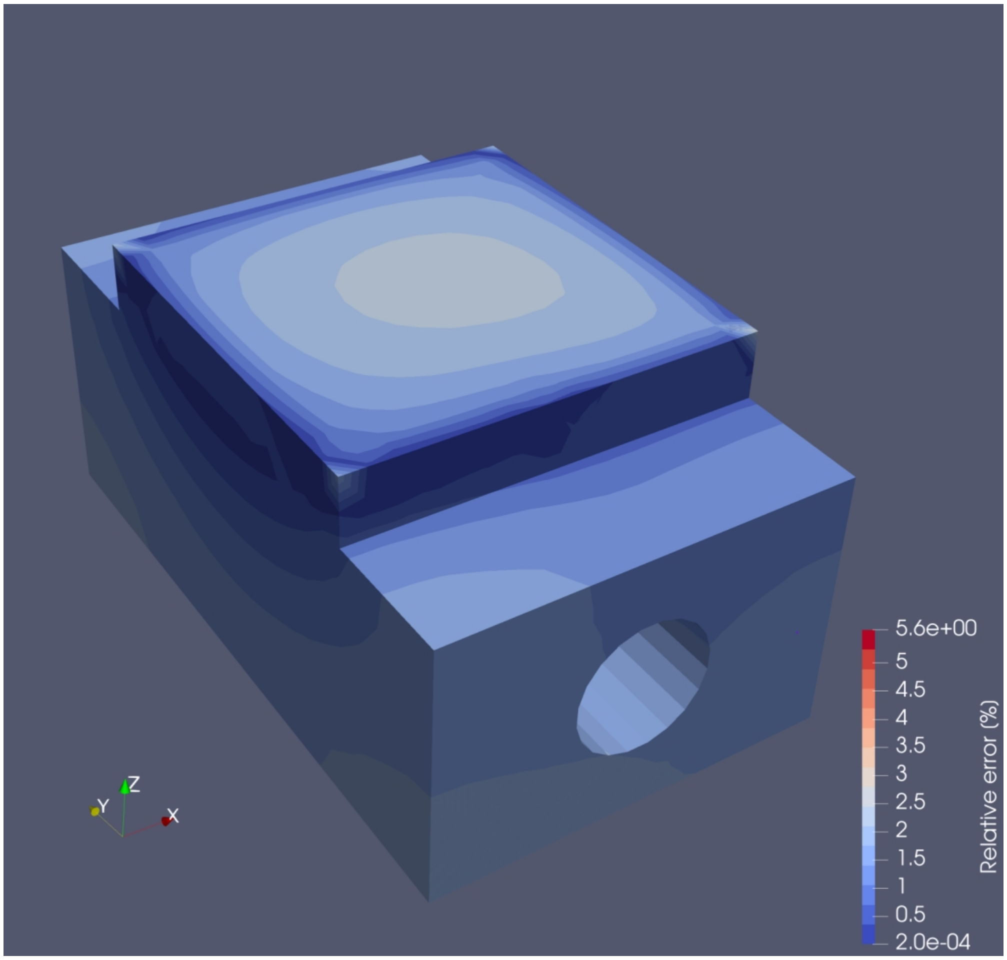

1531x1458mm (28 x 28 DPI)

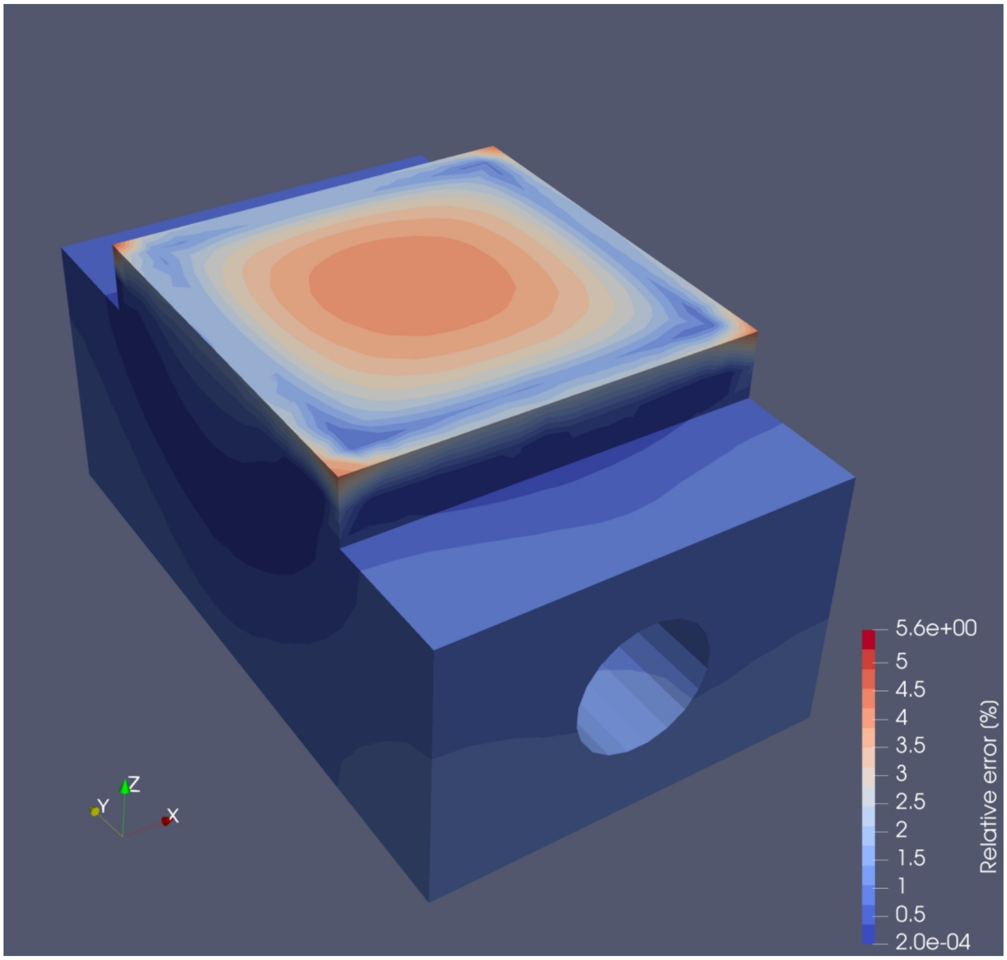

1531x1458mm (28 x 28 DPI)

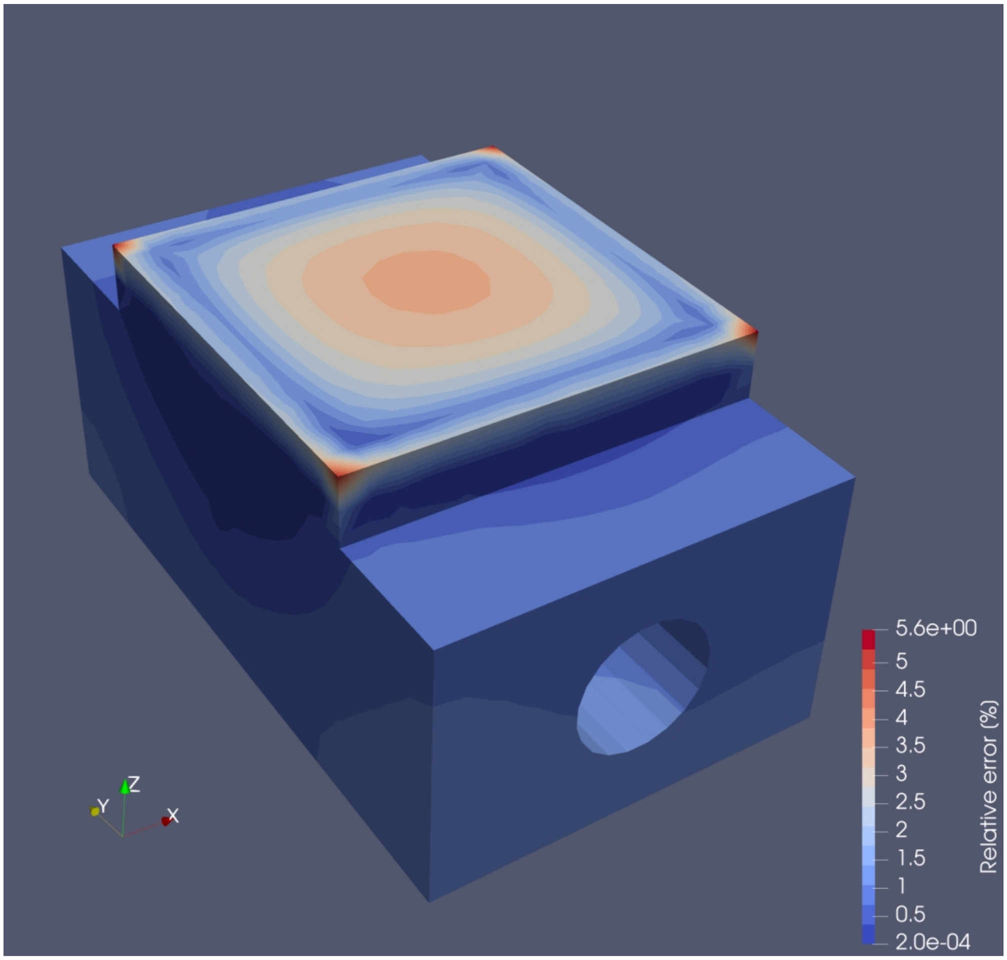

1531x1458mm (28 x 28 DPI)

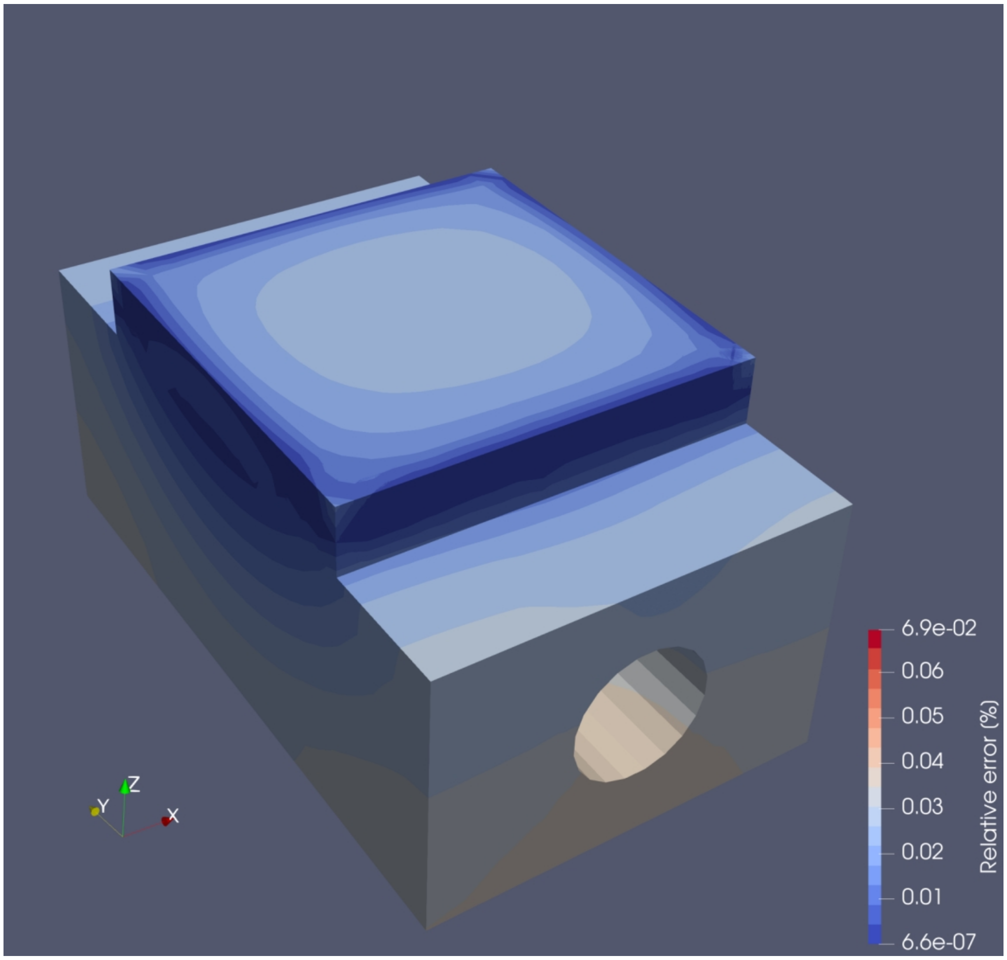

1531x1458mm (28 x 28 DPI)

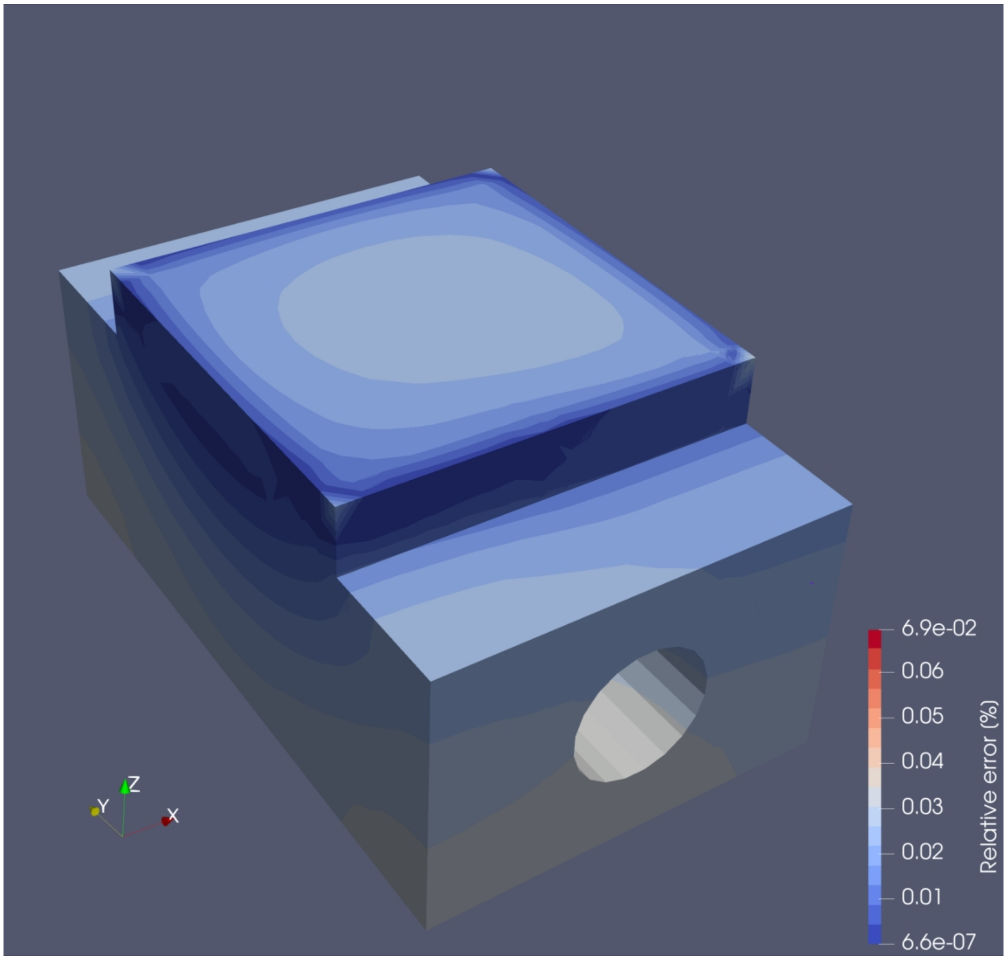

1531x1458mm (28 x 28 DPI)

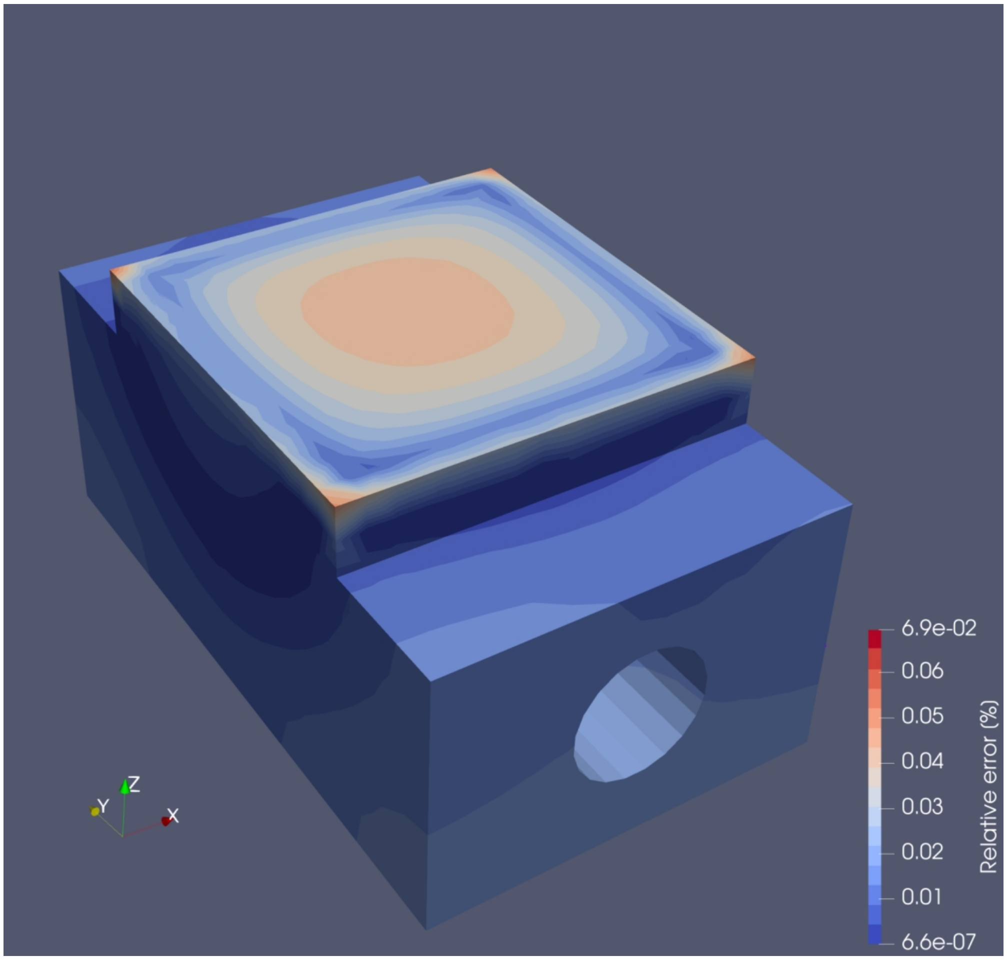

1531x1458mm (28 x 28 DPI)

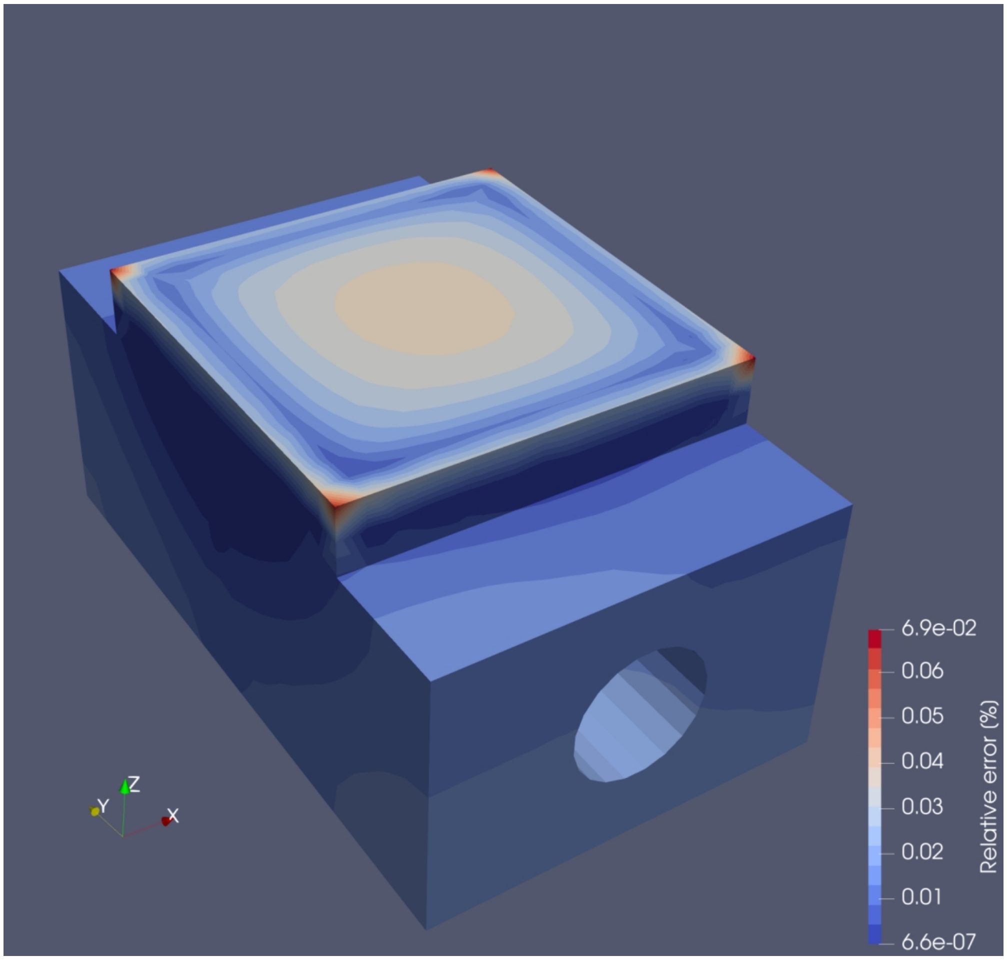

1531x1458mm (28 x 28 DPI)

A novel finite-element-based solution and property construction method for thermal problems from sparse data

---

Abstract

Sparse experimental measurements from diagnostic sensors are often the only source of data available during an experiment. To enable monitoring and control of such experiments (digital twinning) rapidly estimating the full field solution and material properties using sparse data may be useful, especially under extreme thermal environments. This paper addresses such a construction procedure using an efficient finite-element-based approach combined with a modified ODIL (Optimizing a DIscrete Loss) concept. A finite element specific regularisation term is added to the loss function to resolve the ill-posedness. The loss function gradients are calculated analytically. The nonlinear material properties are constructed as a piecewise linear function during the temperature change. A sample from fusion energy experimental facility is used as the test case to demonstrate the proposed methodology. The results indicate that near real-time solution construction is possible, which makes this approach suitable for digital twinning.

Keywords: Solution construction, material properties, sparse data, finite element method, ODIL concept, nuclear fusion, digital twinning

---

1. Introduction

Digital twins and digital twinning are useful in monitoring, controlling, finding faults, and maintaining engineering systems. This recent trend requires a dynamic virtual representation of a physical system to extract useful real-time information to understand and support the physical asset. Such a dynamic virtual representation of the physical system is its digital twin. The real-time data from the physical asset continuously updates the digital twin to fully and accurately simulate its current behaviour [1]. When the information continuously flows between physical asset and its digital twin (monitor-

Preprint submitted to International Journal of Numerical Methods for Heat & Fluid Flow October 10, 2025

ing) and vice versa (control), the process is referred to as digital twinning. It aims to enhance the sparse experimental measurements to provide information for system monitoring and optimising experimental conditions. Ideally, such feedback needs to take place in real-time. This poses a significant challenge in engineering problems that are driven by changing physics. The first step is therefore to rapidly construct full solution and properties (if applicable) from sparse data. This is the topic of the present work.

Construction of full solution and nonlinear properties from sparse solution requires some form of inverse modelling. Historically, inverse problems have primarily focused on estimating parameters in differential equations, with some traditional approaches including functional analytic regularization and statistical regularization [2, 3]. One of the most well-known statistical methods is Bayesian inversion [3]. Alternatively, inverse problems can be solved using search-and-optimization techniques, such as the Particle Swarm Optimization (PSO) algorithm [4]. Comprehensive overviews of various inverse problem-solving methods can be found in the works of Tamaddon-Jahromi et al. [5] and Arridge et al. [3].

However, these traditional techniques often become computationally impractical and generally lack flexibility. Therefore, in recent years, Machine Learning (ML) has been increasingly applied across various engineering disciplines, from manufacturing [6] to aerospace [7]. It offers a combination of unique advantages, such as accuracy, flexibility, efficiency, and scalability [8]. These qualities are highly valued in many engineering applications. Nevertheless, when used for inverse analysis and digital twinning, ML models also present certain limitations.

Data-driven ML models typically require large amounts of training data to achieve sufficient accuracy. While certain ML approaches, such as Gaussian Process Regression (GPR) [9], require considerably less data compared to other models like Neural Networks (NNs) [10, 11], Long Short-Term Memory (LSTM), and Transformers [12], a substantial dataset is still necessary. This presents a major challenge in complex engineering applications, where acquiring large volumes of data is difficult. There are two main ways to address this issue: (1) Utilizing experimental data for training or (2) Generating training data through numerous forward simulations, such as Finite Element Method (FEM) simulations [5, 12, 13, 14, 15, 16]. The former option is rarely feasible in engineering since experimental data is often sparse and insufficient for effectively training a data-driven ML model. The latter approach appears more viable but relies on having a fully accurate, verified, and reliable FEM model, which is a complex task of its own, particularly when dealing with extreme environments. Moreover, training the ML model on a limited set of forward simulations can introduce bias, leading to predictions that might not necessarily match the physical experiment. Reinforcement Learning could be used to create a DT of a thermal system and control the temperature through heat transfer coefficient adjustment [17]. It is more flexible as compared with the aforementioned data-driven supervised learning approach but requires more computational resources due to the interactive learning.

In contrast, physics-based ML models, the most popular one being Physics-Informed Neural Networks (PINNs), do not depend on training data. Instead, they are trained directly using the governing partial differential equations (PDEs) [18, 19]. However, Optimizing a DIscrete Loss (ODIL) approach proved to be significantly more efficient than PINNs [20, 21]. ODIL integrates discretization techniques, such as finite volume (FV), with ML-inspired optimization strategies. Automatic differentiation is used to calculate the Jacobian matrices; and unknown material properties are represented using NNs.

Thus, this paper uses a modification of ODIL tailored to the finite element method (FEM). The finite element specific regularisation term is introduced to the loss function, which is used in conjunction with Neumann boundary conditions (BCs). Loss function gradients are derived analytically and the material properties are constructed as a piecewise linear function. The AMAZE (Additive Manufacturing Aiming towards Zero waste and Efficient production of high-tech metal products) sample from fusion experimental facility is used as the test case. This sample was previously tested in fusion energy experimental facility [22, 23].

The remainder of the paper is organised into following sections. Section 2 details the methodology. Section 3 presents and interprets the results for several thermal field and thermal conductivity construction cases. Finally, Section 4 summarises the significance of the results.

2. Methodology

After discretising a general transient heat conduction equation without a heat source in space using the standard Galerkin weighted residual method, the following system of equations is obtained:

$$[\boldsymbol{M}]\left\{\frac{\Delta \boldsymbol{T}}{\Delta t}\right\}+[\boldsymbol{K}]\{\boldsymbol{T}\}^{n+1}=\{\boldsymbol{f}\}^{n+1} \tag{1}$$

where $\Delta\boldsymbol{T}=\{\boldsymbol{T}\}^{n+1}-\{\boldsymbol{T}\}^{n}$, $[\boldsymbol{M}]$ and $[\boldsymbol{K}]$ are global mass and stiffness matrices, respectively. And $\{\boldsymbol{T}\}$ and $\{\boldsymbol{f}\}$ are temperature and global loading, respectively. Superscript n represents the n^{th} time step, Δt is a time step size. Global loading $\{\boldsymbol{f}\}$ may be decomposed into $\{\boldsymbol{f}\}_q$ and $\{\boldsymbol{f}\}_{g-q}$, where $\{\boldsymbol{f}\}_q$ is a part of the loading term vector corresponding to the applied heat flux q on Γ_q and $\{\boldsymbol{f}\}_{g-q}$ is the rest of the loading vector including the convection with the heat transfer coefficient h on Γ_h. First-order implicit Euler time discretization scheme is adopted.

Assuming that the heat flux boundary conditions are unknown in Eq. 1, the above system of equations may be decomposed into two sets:

$$\begin{bmatrix}[\boldsymbol{M}]_q\\ [\boldsymbol{M}]_{g-q}\end{bmatrix}\left\{\frac{\Delta \boldsymbol{T}}{\Delta t}\right\}+\begin{bmatrix}[\boldsymbol{K}]_q\\ [\boldsymbol{K}]_{g-q}\end{bmatrix}\{\boldsymbol{T}\}^{n+1}-\begin{Bmatrix}\{\boldsymbol{f}\}_q\\ \{\boldsymbol{f}\}_{g-q}\end{Bmatrix}^{n+1}=0 \tag{2}$$

Subscript q indicates all terms in Eq. 1 corresponding to the nodes belonging to Γ_q, whereas subscript $g-q$ indicates all equations corresponding to the nodes belonging to $\Omega\setminus\Gamma_q$. Ω is the whole domain.

The second part of Eq. 2 consists of convective or any other known boundary condition and is capable for determining temperature values everywhere including boundaries on which heat fluxes are unknown. Applied heat flux can be determined from the constructed temperature distribution $\{\boldsymbol{T}\}_{con}$ at each time step using the following equation:

$$q_{con}^{n}=\frac{\int_{\Gamma_q}\boldsymbol{n}k(T)\nabla T_{con}^{n}d\Gamma}{\int_{\Gamma_q}1d\Gamma} \tag{3}$$

where $\boldsymbol{n}$ is a vector normal to Γ_q and q_{con} is the heat flux on Γ_q constructed from $\{\boldsymbol{T}\}_{con}$.

If measured temperature is available on selected points and some boundary conditions are unknown, the problem becomes a minimization problem consisting of known temperatures at certain points and the second part of Eq. 2. We often refer to this process as inverse calculation of boundary conditions. For such inverse analysis it is assumed that the ambient temperature, as well as temperature values $\{\boldsymbol{T}\}_M$ at points belonging to a measurement set

M are known. The applied heat flux q is assumed to be unknown. Rewriting Eq. 2 as:

$$\left\{ \begin{matrix} \{\boldsymbol{f}\}_q \\ \{\boldsymbol{R}\}_{g-q} \end{matrix} \right\}^{n+1} = \begin{bmatrix} [\boldsymbol{M}]_q \\ [\boldsymbol{M}]_{g-q} \end{bmatrix} \left\{ \frac{\Delta \boldsymbol{T}}{\Delta t} \right\} + \begin{bmatrix} [\boldsymbol{K}]_q \\ [\boldsymbol{K}]_{g-q} \end{bmatrix} \{\boldsymbol{T}\}^{n+1} - \left\{ \begin{matrix} 0 \\ \{\boldsymbol{f}\}_{g-q} \end{matrix} \right\}^{n+1} \tag{4}$$

Before computing the boundary load on Γ_q, it is necessary to find the vector of unknown nodal temperatures and material properties; all unknown parameters are represented by vector $\{\boldsymbol{v}\}$. To compute $\{\boldsymbol{v}\}$, the magnitude of a loss vector $\{\boldsymbol{L}\}$ depending on $\{\boldsymbol{v}\}$ is minimized. The loss vector is defined as:

$$\{\boldsymbol{L}\} = \left\{ \begin{matrix} \{\boldsymbol{L}\}_R \\ \{\boldsymbol{L}\}_M \\ \{\boldsymbol{L}\}_{REG} \end{matrix} \right\} \tag{5}$$

The residual component is calculated as (Eq. 4):

$$\{\boldsymbol{L}\}_R = \{\boldsymbol{R}\}_{g-q} \tag{6}$$

The measurement component is calculated as

$$\begin{aligned} \{\boldsymbol{L}\}_M &= \{\boldsymbol{s}\}_M \odot (\{\boldsymbol{T}\}_i - \{\boldsymbol{T}\}_{Mi}) \\ \{\boldsymbol{s}\}_{Mi} &= \begin{cases} 1, & \text{if } i \in M \\ 0, & \text{if } i \notin M \end{cases} \end{aligned} \tag{7}$$

where $\odot$ is Hadamard (or element-wise) product.

The regularisation (smoothing) component is calculated at each iteration using the first part of Eq. 4 as:

$$
\{\boldsymbol{L}\}_{REG} = \left\{ \begin{array}{c} \{\boldsymbol{s}\}_1 \odot \left(\{\boldsymbol{f}\}_q - \frac{\sum_{i \in \Gamma_q \setminus \Gamma_{edge}} \{\boldsymbol{f}\}_{qi}}{\left|\Gamma_q \setminus \Gamma_{edge}\right|} \right) \\ \{\boldsymbol{s}\}_2 \odot \left(\{\boldsymbol{f}\}_q - \frac{\sum_{i \in \Gamma_{edge} \setminus \Gamma_{corners}} \{\boldsymbol{f}\}_{qi}}{\left|\Gamma_{edge} \setminus \Gamma_{corners}\right|} \right) \\ \{\boldsymbol{s}\}_3 \odot \left(\{\boldsymbol{f}\}_q - \frac{\sum_{i \in \Gamma_{corners}} \{\boldsymbol{f}\}_{qi}}{\left|\Gamma_{corners}\right|} \right) \end{array} \right\}
$$

$$
\{\boldsymbol{s}\}_{1i} = \begin{cases} 1, & \text{if } i \in \Gamma_q \setminus \Gamma_{edge} \\ 0, & \text{if } i \notin \Gamma_q \setminus \Gamma_{edge} \end{cases}
$$

$$
\{\boldsymbol{s}\}_{2i} = \begin{cases} 1, & \text{if } i \in \Gamma_{edge} \setminus \Gamma_{corners} \\ 0, & \text{if } i \notin \Gamma_{edge} \setminus \Gamma_{corners} \end{cases}
$$

$$
\{\boldsymbol{s}\}_{3i} = \begin{cases} 1, & \text{if } i \in \Gamma_{corners} \\ 0, & \text{if } i \notin \Gamma_{corners} \end{cases} \tag{8}
$$

Γ_{edge} is the 3D edge of the surface where q is applied, and sharp features on Γ_{edge} discretised using single element are represented by $\Gamma_{corners}$. Time dependent term in Eqs. 1, 2, and 4 can be ignored for the steady state solution.

The magnitude of $\{\boldsymbol{L}\}$, $\|\{\boldsymbol{L}\}\|$, can be minimized using gradient-based optimisation approach, which is the Gauss-Newton method in this paper [24, 25]. $\|\{\boldsymbol{L}\}\|^2$ is a sum of squared function values, i.e. $\|\{\boldsymbol{L}\}\|^2 = \sum l_i^2$, and it is necessary to calculate their Jacobian matrices $[\boldsymbol{J}]_{ij} = \partial l_i / \partial \{\boldsymbol{v}\}_j$ for every iteration of the minimizer. For the loss vector derived from the FE equations, $[\boldsymbol{J}]$ can be calculated analytically. $\|\{\boldsymbol{L}\}\|$ is minimized by evaluating $[\boldsymbol{J}]$ and $\{\boldsymbol{L}\}^s$ at every iteration s and solving the following system of equations to find $\Delta\{\boldsymbol{T}\}$:

$$
\begin{aligned} [\boldsymbol{J}]^T [\boldsymbol{J}] \Delta \{\boldsymbol{T}\} &= -[\boldsymbol{J}]^T \{\boldsymbol{L}\}^s \\ \{\boldsymbol{T}\}^{s+1} &= \{\boldsymbol{T}\}^s + \Delta \{\boldsymbol{T}\} \end{aligned} \tag{9}
$$

2.1. Solution construction

When performing the solution construction from sparse temperature measurements assuming that the material properties are known, the vector of unknown variables becomes the following:

$$
\{\boldsymbol{v}\} = \{\boldsymbol{T}\} = [T_1, T_2, \ldots, T_N]^T \tag{10}
$$

2.2. *Linear material properties*

This subsection describes the linear material properties construction process from sparse temperature measurements within the domain. Assuming the domain consisting of one linear material with thermal conductivity k, the vector of unknown variables becomes the following:

$$\{\boldsymbol{v}\} = [T_1, T_2, \ldots, T_n, k]^T \tag{11}$$

Extra column is added to $[\boldsymbol{J}]$ corresponding to $\partial l_i/\partial k$.

When the domain consists of two materials with thermal conductivities k_1 and k_2, the vector of unknowns is the following:

$$\{\boldsymbol{v}\} = [T_1, T_2, \ldots, T_n, k_1, k_2]^T \tag{12}$$

Two extra column corresponding to $\partial l_i/\partial k_1$ and $\partial l_i/\partial k_2$ are added to $[\boldsymbol{J}]$.

2.3. *Nonlinear material properties*

This subsection describes the nonlinear material properties construction process from sparse temperature measurements within the domain.

2.3.1. *Linear temperature dependency*

It is assumed that a domain consists of one material, and a following linear relationship between k and T is observed:

$$k(T) = aT + b \tag{13}$$

Furthermore, it is assumed that it is known that k is equal to k_{known} at T_{known}. Consequently, Eq. 13 can be re-written as:

$$k(T) = aT + (k_{known} - aT_{known}) \tag{14}$$

Hence, the vector of unknown variables becomes the following:

$$\{\boldsymbol{v}\} = [T_1, T_2, \ldots, T_n, a]^T \tag{15}$$

Extra column is added to $[\boldsymbol{J}]$ corresponding to $\partial l_i/\partial a$, which are computed using Eq. 16 following from Eq. 14:

$$\frac{\partial k}{\partial a} = T - T_{known} \tag{16}$$

2.3.2. *Piecewise linear temperature dependency*

When it is assumed that $k(T)$ is known for temperatures T below or equal to T_r, Eq. 17 can be used to represent $k(T)$ for temperatures T above T_r:

$$k(T) = aT + (k_r - aT_r) \tag{17}$$

Since $k(T)$ below or equal to T_r is assumed to be already known, then the conductivity k_r at T_r is known. Therefore, new parameter a could be constructed to determine $k(T)$ for $T > T_r$ using Eq. 17. Figure 1 illustrates the process.

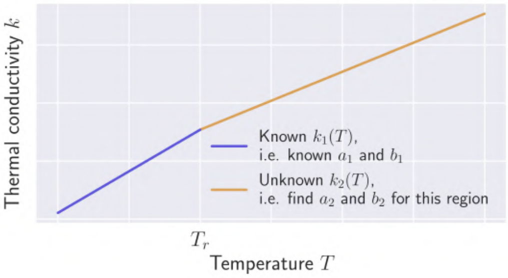

Figure 1: Construction of linear $k(T)$ with known $k(T)$ for $T \leq T_r$. Source: By authors.

The aforementioned approach to construct linear $k(T)$ knowing one point (T_{known}, k_{known}) and the approach to construct linear $k(T)$ with known $k(T)$ for $T \leq T_r$ can be combined; and a piecewise linear relationship between k and T can be derived from one known point (T_{known}, k_{known}). Figure 2 summarises the procedure, which can be performed as test piece heats up. $k(T)$ is constructed as a piecewise linear function, thus T_{r1}, T_{r2}, T_{r3} etc represent the defined transition temperatures for each linear segment of $k(T)$. Linear segment 1 is between T_{r1} and T_{r2}, linear segment 2 is between T_{r2} and T_{r3}.

3. Results and discussion

3.1. *AMAZE sample*

This paper uses a water-cooled AMAZE sample, previously tested in the fusion energy experimental facility [22, 23], as an example of nonlinear heat conduction. Table 1 and Figure 3 describe the applied BCs. A uniform linear hexahedral mesh with the second-order Gaussian quadratures created in Ansys [26] is comprised of 5,185 elements. FE model is created using Netgen/NGSolve solver [27]. Water-pipe convection heat transfer coefficient h_c is calculated using a 1D coolant model [28], with water pressure p_c and

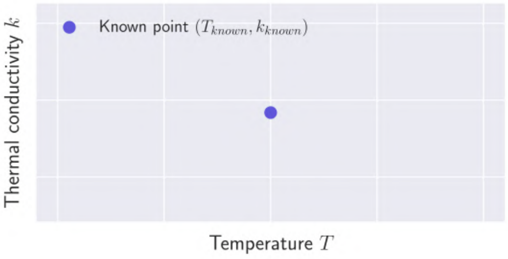

(a) Known point (T_{known}, k_{known}).

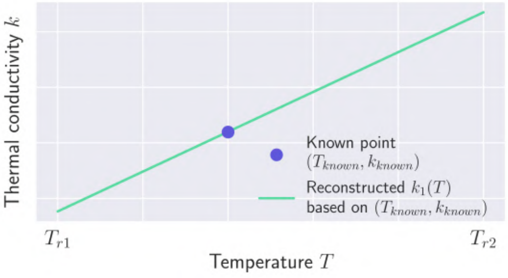

(b) Start and end temperatures for the first linear piece, T_{r1} and T_{r2}, respectively, are defined. The first linear piece $k_1(T)$ is constructed using (T_{known}, k_{known}).

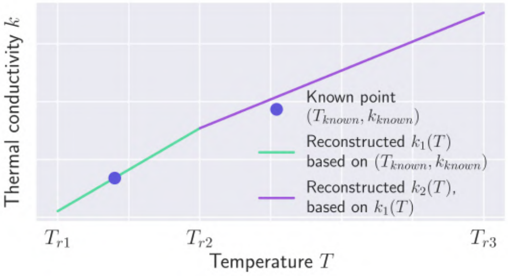

(c) Start and end temperatures for the second linear piece, T_{r2} and T_{r3}, respectively, are defined. The second linear piece $k_2(T)$ is constructed using $k_1(T)$.

Figure 2: Construction of piecewise linear relationship between k and T from one known point (T_{known}, k_{known}). Source: By authors.

temperature T_c remaining constant at 30°C and 1 atm, respectively. This 1D coolant model is defined using water's boiling curve, which represents the influence pipe wall temperature has on the heat flux between the water and pipe. This correlation is split between forced convection regime and nucleate boiling regime with details provided by Marshall et al. [28], Seibold et al. [29], and Araki et al. [30].

Water-pipe convection heat transfer coefficient h_c depends on the temperature distribution on the surface of a pipe. Coolant velocity v_c and uniform heat flux q, applied to the tile's top surface, are varied to achieve temperature distributions within various boundaries. Figure 4 shows temperature measurement locations used in this work.

Table 1: Applied BCs for AMAZE sample with Figure 3 showing the labels. Source: By authors.

Surface	**BC**
ABCD	Uniform heat flux q
Pipe surface	Sample-coolant (water) convection h_c
Set	**Location**
Γ_q	Surface ABCD
Γ_{edge}	Edge ABCD
$\Gamma_{corners}$	Nodes A, B, C, D
Tile	ABCDHEFG
Block	IJKLPMNO
Volume	**Material for Subsection 3.2**
Tile ABCDHEFG	Tungsten (Figure 5)
Block IJKLPMNO	Copper (Figure 5)
Pipe	Copper (Figure 5)

3.2. 3D transient solution construction

This section describes the results obtained by constructing the full field temperature distribution within the sample from transient temperature measurements from 4, 8, 11, and 17 locations shown in Figure 4. It is assumed that the sample consists of two nonlinear materials: copper with thermal

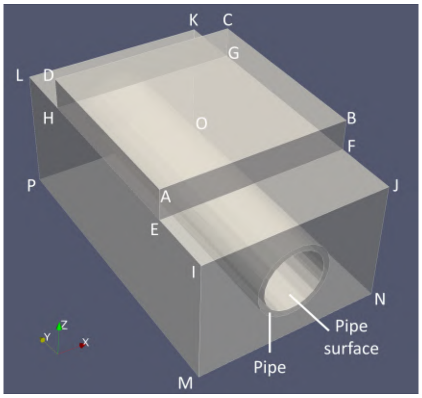

Figure 3: AMAZE sample geometry with labels (Table 1). Source: By authors.

conductivity k_c and volumetric heat capacity $(\rho c_p)_c$ on the block and tungsten with k_t and $(\rho c_p)_t$ on the tile (Figure 3). Figure 5 shows temperature dependency of the material properties. Applied heat flux $q(t)$ is defined by Eq. 18; coolant velocity v_c is set to 10 m/s.

$$q(t) = \left(\frac{5}{180}\right) t \quad [MW/m^2] \tag{18}$$

The time step size used for solution construction Δt_{con} is equal to 2.8s, while the time step size used for reference solution Δt_{ref} is equal to 0.4s. The optimisation is preformed for 3 iterations in order to ensure that the solution construction is close to real time. The initial temperature field is defined as a uniform distribution of 30°C, corresponding to the steady-state condition aligned with the coolant temperature.

In addition, noise is introduced into the temperature measurements to evaluate the robustness of the solution setup. The noise is generated as random values from a zero-mean Gaussian distribution, with the standard deviation representing the measurement precision (noise level). This noise level is presented as a percentage of the true temperature, and it determines the standard deviation of the distribution. Table 2 summarises the specific noise levels considered in this work.

Figure 6 shows the precision characteristic $\sigma(T)$ of Type K thermocouple measurements dependent on the temperature. The uncertainty is shown in °C and also as a percentage of the measured temperature [31].

Table 2: Noise settings presented as a true temperature value percentage. Source: By authors.

Noise setting No.	**Noise level (measurement precision)** $\boldsymbol{\sigma}$ [%]
1	0.0
2	0.2
3	1.0
4	$\sigma(T)$

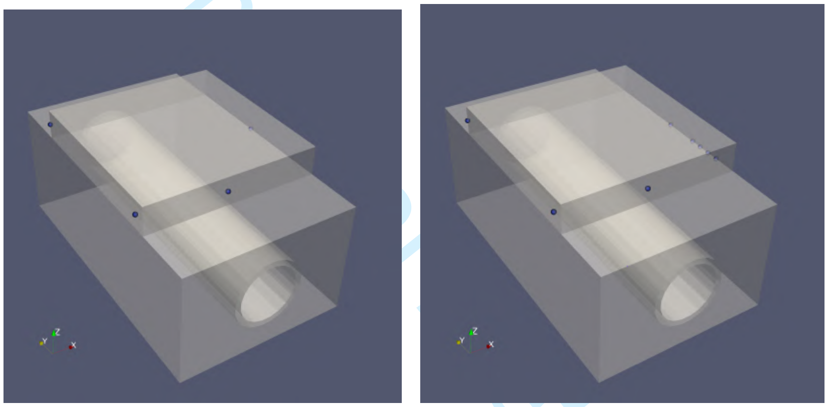

(a) 4 measurement locations. (b) 8 measurement locations.

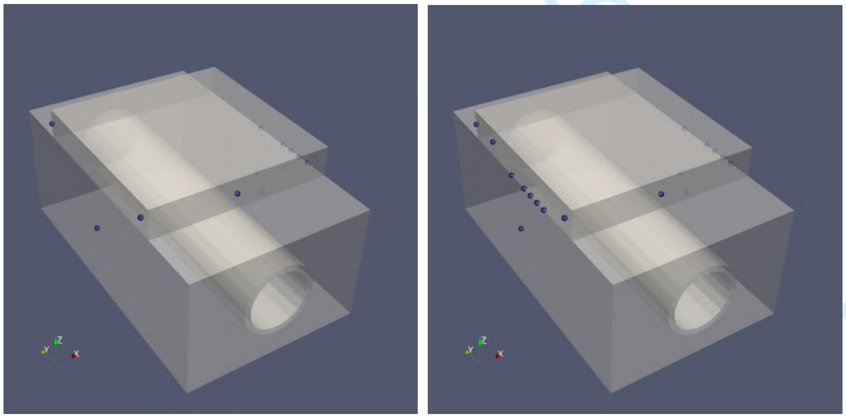

(c) 11 measurement locations. (d) 17 measurement locations.

Figure 4: Measurement locations shown as blue spheres. Source: By authors.

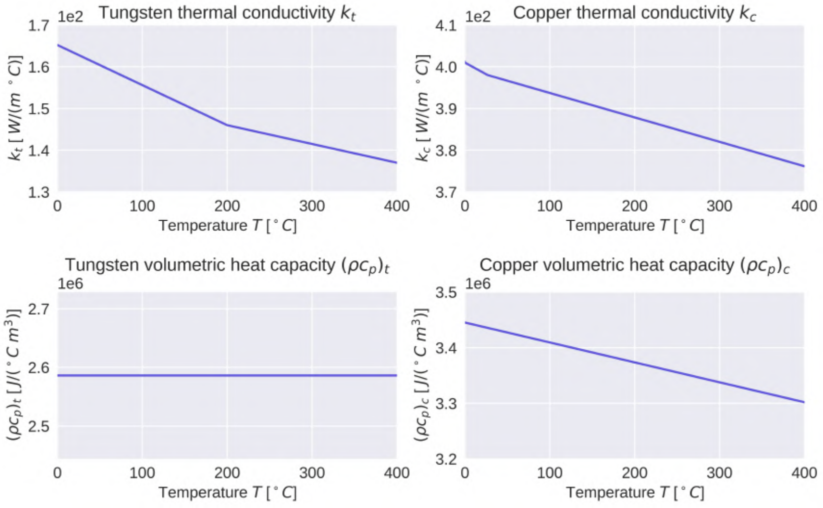

Figure 5: Copper and tungsten nonlinear material properties. Source: By authors.

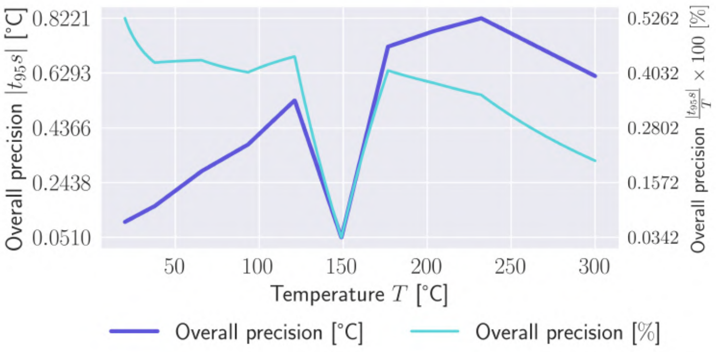

Figure 6: The precision of a standard type K thermocouple $\sigma(T)$ dependent on the true temperature. [31]. Source: By authors.

Table 3 reports the solution construction errors and time step runtimes. The listed average and maximum errors are evaluated over both space and time. It is important to consider the solution construction time when selecting the appropriate time step size for the reconstruction process. The construction time should be less than or equal to the chosen solution construction time step to ensure that the control procedure operates in near real time with a consistent delay. Accordingly, Table 3 confirms that, for the selected time step size, the solution construction process indeed functions in near-real time.

Table 3: Time step runtimes and solution construction errors for the FE-based solution construction. Source: By authors.

		Sol. rec. time		**Sol. rec. errors**	
No. of measurement locations	**Noise level σ** [%]	Avg. time step runtime [s] [a]	Max. time step runtime [s] [a]	Avg. relative error [%]	Max. relative error [%]
4	0.0	2.306	3.038	0.282	2.196
4	0.2	2.347	2.495	0.353	4.55
4	1.0	2.278	2.433	0.734	19.222
4	$\sigma(T)$	2.265	2.376	0.421	8.267
8	0.0	2.297	2.515	0.263	2.423
8	0.2	2.244	2.379	0.303	6.173
8	1.0	2.299	2.411	0.553	21.164
8	$\sigma(T)$	2.276	2.463	0.342	10.433
11	0.0	2.279	2.419	0.177	4.858
11	0.2	2.253	2.441	0.229	5.629
11	1.0	2.261	2.387	0.514	18.008
11	$\sigma(T)$	2.303	2.615	0.277	7.655
17	0.0	2.311	2.452	0.174	5.584
17	0.2	2.259	2.429	0.23	7.321
17	1.0	2.286	2.404	0.522	23.951
17	$\sigma(T)$	2.277	2.432	0.283	9.316

[a] Times are given for AMD Ryzen 7 5800X 8-Core CPU.

As expected, with a fixed number of measurement locations, higher noise levels result in larger relative construction errors. This trend is illustrated in Figures 7 and 8, which show how the maximum and average relative errors evolve over time. The errors rise sharply at the beginning of the simulation, peaking around 8.4s. This behaviour can be linked to the transition of the temperature field from its uniform initial state of 30°C to a distribution influenced by the applied heat flux. Because the heat flux increases rapidly, this early stage involves strong spatial and temporal variations in temperature. The relatively large time step used in constructing the solution reduces

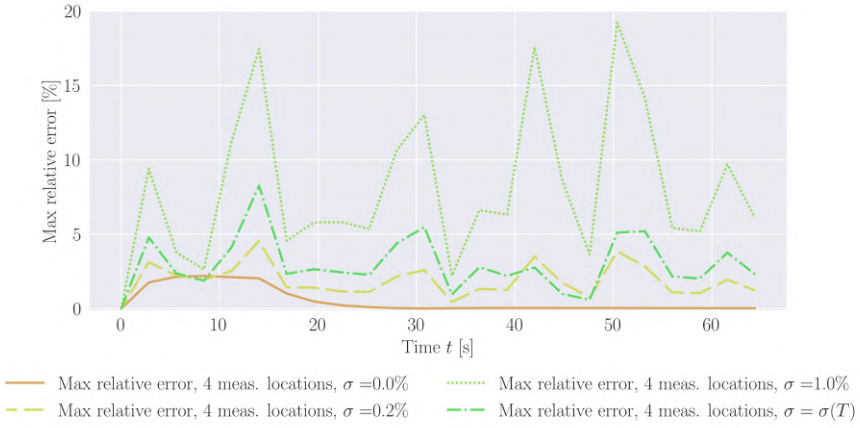

(a) 4 measurement locations

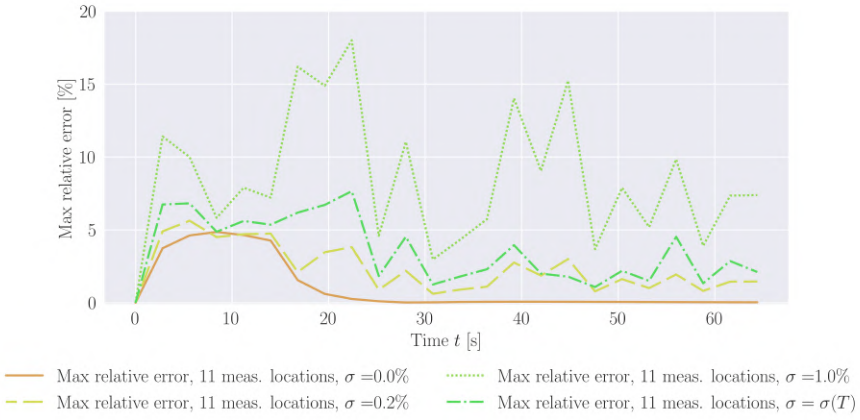

(b) 11 measurement locations

Figure 7: The time evolution of maximum relative errors for 4 and 11 measurement locations (Figure 4). Source: By authors.

its ability to capture these rapid changes, leading to the initial error spike. After 20s, however, the errors diminish.

The presence of noise causes increasingly sharp fluctuations in both the maximum and average relative errors, indicating that additional measurement points are needed to lessen its impact. In fact, increasing the number of measurement locations generally leads to a reduction in the average relative construction error (Table 3 and Figure 8), particularly during the initial temperature transition period before 20s, where the errors are most pro-

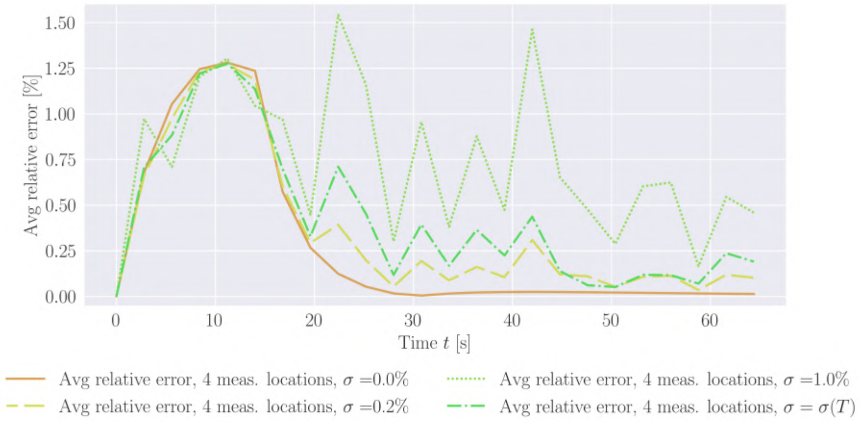

(a) 4 measurement locations

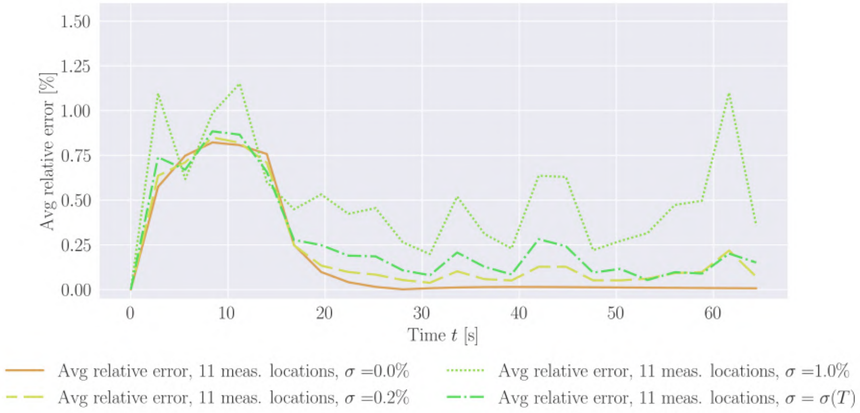

(b) 11 measurement locations

Figure 8: The time evolution of average relative errors for 4 and 11 measurement locations (Figure 4). Source: By authors.

nounced. Nevertheless, the maximum relative error does not consistently decrease with more measurement points. Over time, the maximum errors tend to oscillate around a similar level or, in some cases, even rise for certain measurement configurations under the same noise conditions (Figure 7).

Examining the spatial distributions of errors helps to clarify this behaviour. Distributions of relative error at two time instances, 8.4s and 50.4s, are presented in Figures 9 and 10. The former corresponds to the peak of maximum relative errors (Figure 7), while the latter illustrates a case with

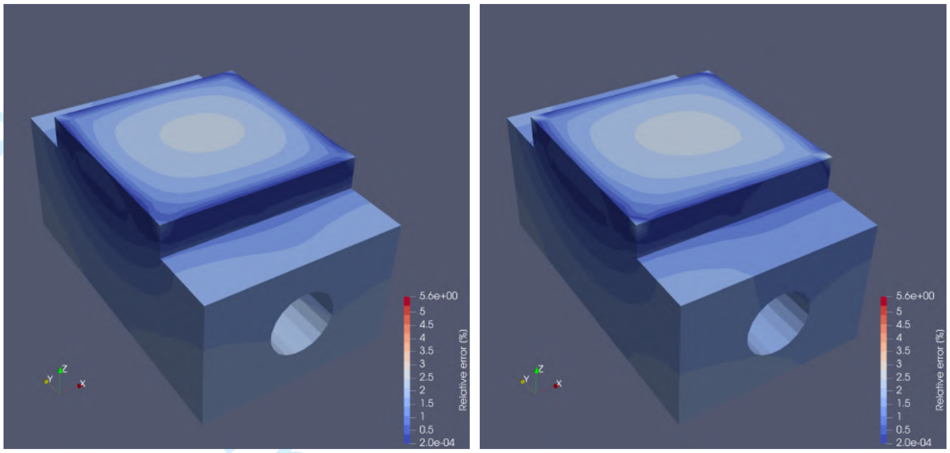

(a) 4 measurement locations (b) 8 measurement locations

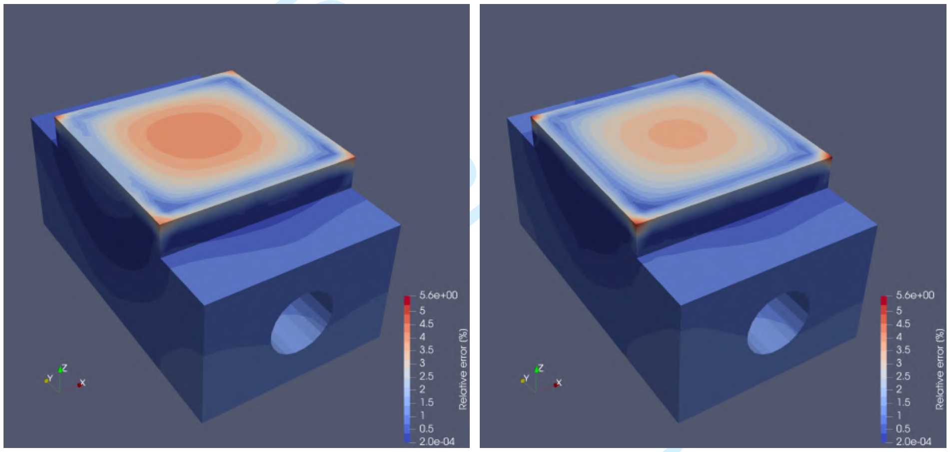

(c) 11 measurement locations (d) 17 measurement locations

Figure 9: Distributions of relative error at $t = 8.4s$; the measurement locations are provided in Figure 4. Source: By authors.

minimal errors. A consistent trend can be observed across both figures. With only 4 or 8 measurement locations, the error distribution remains fairly uniform and dominated by low values, with most of the domain exhibiting small errors. By contrast, increasing the number of measurement locations to 11 and 17 alters the distribution markedly: areas of higher relative error emerge near the upper surface of the tile, especially at the corners, while errors within the block, the pipe, and most of the tile are reduced. Thus, although adding more measurement points generally lowers the average error, the im-

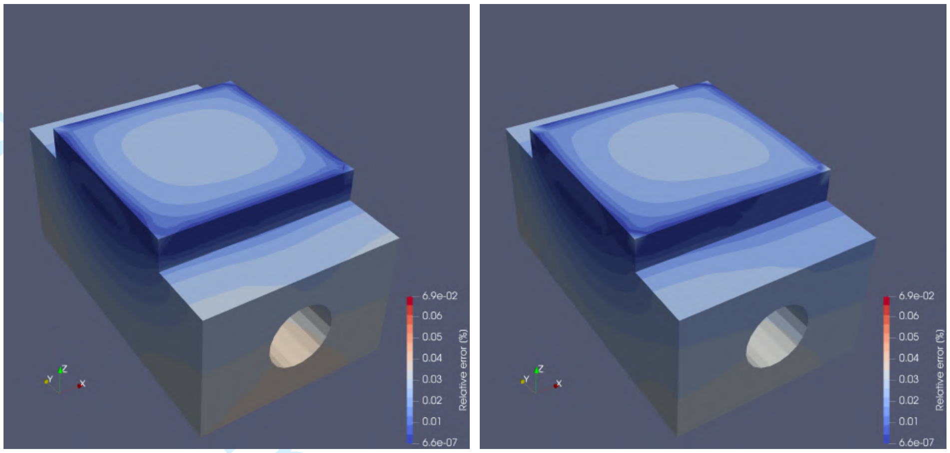

(a) 4 measurement locations (b) 8 measurement locations

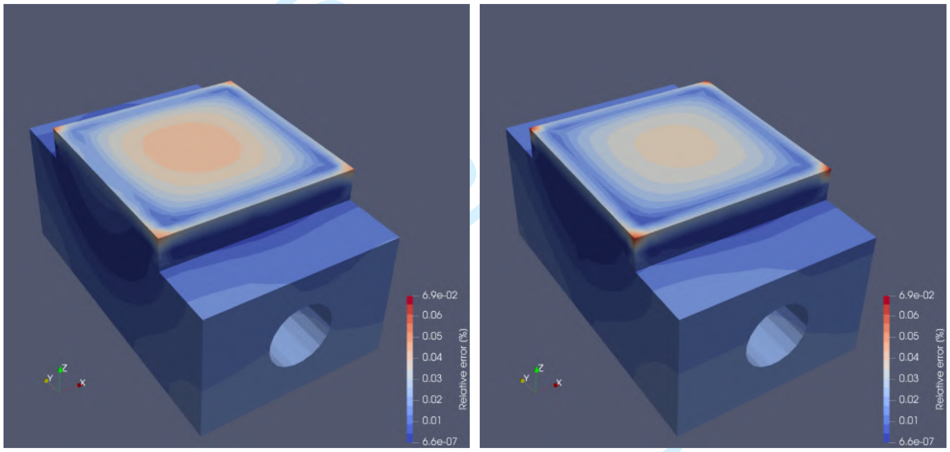

(c) 11 measurement locations (d) 17 measurement locations

Figure 10: Distributions of relative error at $t = 50.4s$; the measurement locations are provided in Figure 4. Source: By authors.

provement is not spatially uniform, and localised regions of higher error may persist.

The temperature field reconstructed from the measurements can be used to derive the corresponding heat flux (Eq. 3). It then can be compared against the reference applied heat flux. Figure 11 illustrates how the constructed heat flux and its relative error evolve over time. The elevated average relative errors during the initial transition phase lead to a pronounced spike in the heat flux error at the start of the simulation, which then rapidly diminishes

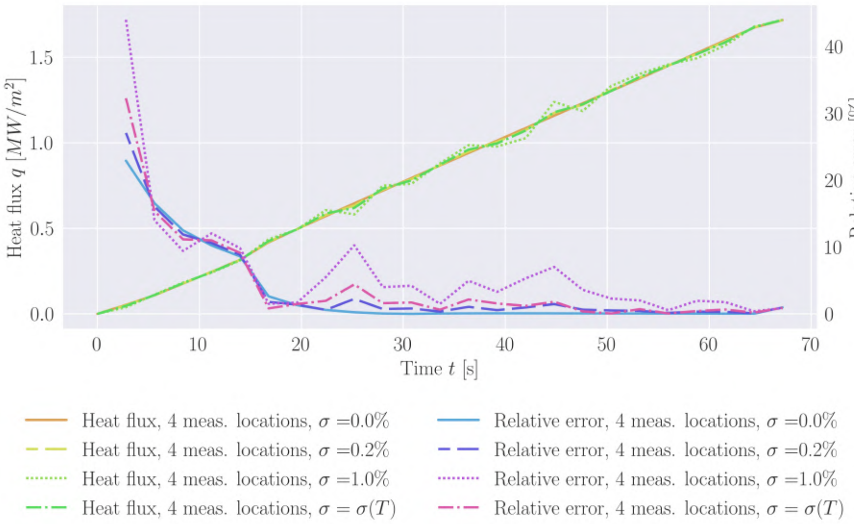

(a) 4 measurement locations

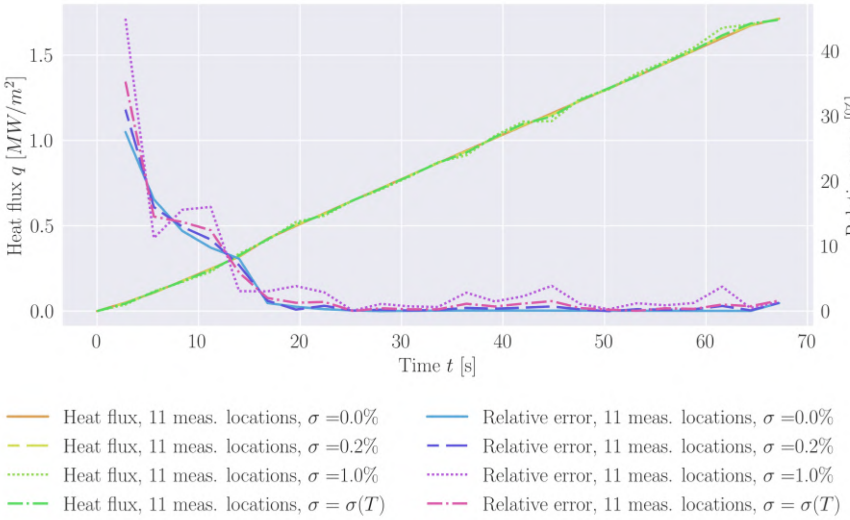

(b) 11 measurement locations

Figure 11: The time evolution of constructed heat flux for 4 and 11 measurement locations (Figure 4). Source: By authors.

as the time approaches 20s. Figure 12 presents the average and maximum relative heat flux errors after 20s, highlighting the advantage of increasing the number of measurement locations (and thereby reducing the average reconstruction error), particularly under higher noise conditions. In general, both the average and maximum relative heat flux errors decrease with more measurement points. This trend is also evident in Figure 11, where the oscillation amplitude of the heat flux error is significantly reduced for larger numbers of measurement locations.

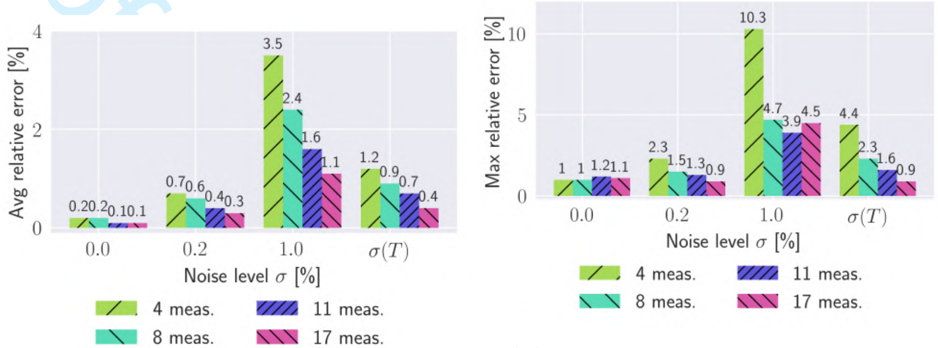

(a) Average relative heat flux error

(b) Maximum relative heat flux error

Figure 12: Relative heat flux errors recorded after 20s. Source: By authors.

3.3. *Thermal conductivity construction from 3D steady-state data*

This sub-section describes the results obtained by constructing linear and nonlinear thermal conductivity from the steady state measurements within AMAZE sample.

3.3.1. *Linear thermal conductivity*

Linear thermal conductivity is constructed using an approach described in Sub-section 2.2. Two cases are considered. First case assumes the sample consists of one material with thermal conductivity k_1. Figure 4a shows 4 locations used to collect the temperature measurements for this case (Figure 4). Second case assumes the sample consists of two materials with thermal conductivity k_1 on the block and k_2 on the tile (Figure 3). Figure 13 shows 5 locations used to collect the temperature measurements for this case. Coolant velocity v_c is set to 1 m/s, while the applied heat flux q is set to 210000 W/m^2.

Figure 14 shows the parameter convergence. The process is stopped when Δk between two subsequent iterations is less than 0.01%. Table 4 lists the

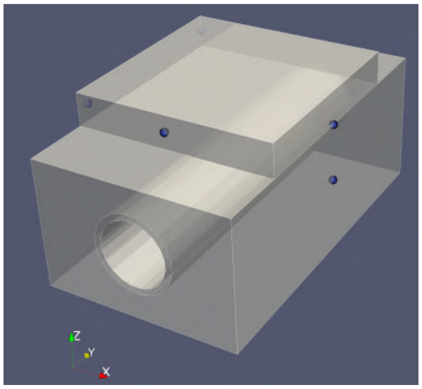

Figure 13: 5 measurement locations used to construct thermal conductivities for the sample consisting of two materials. Source: By authors.

results, from which it can be seen that the linear thermal conductivity and the corresponding solutions are successfully constructed.

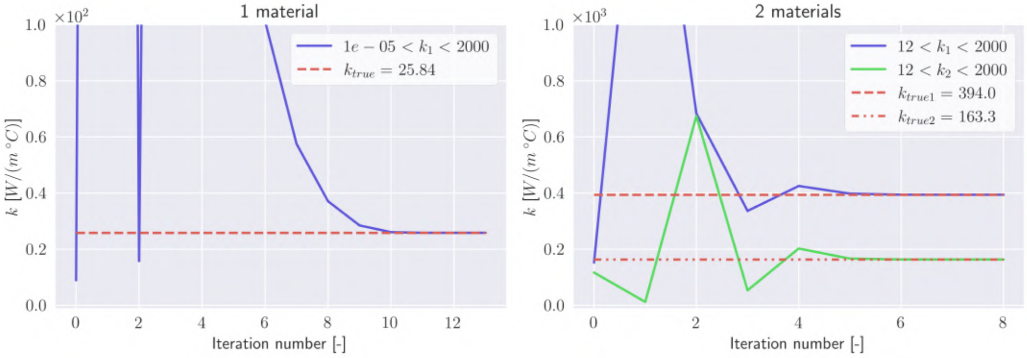

Figure 14: Convergence of a for four linear sections (Figure 15 and Table 5). Source: By authors.

3.3.2. Nonlinear thermal conductivity

A more in-depth analysis is conducted for the nonlinear thermal conductivity reconstruction. This analysis examines how the number of measurement locations (Figure 4) and the noise level (Table 2) affect the performance of the construction process. This set of measurement locations is used for the analysis of the solution construction process in Sub-section 3.2. Piecewise linear thermal conductivity shown in Figure 15 is constructed using an ap-

Table 4: Linear thermal conductivity construction results. Source: By authors.

Case	k_1 **error** [%]	k_2 **error** [%]	**Avg.** $\{T\}$ **error** [%]	**Max.** $\{T\}$ **error** [%]
1 material	2.13E-03	-	9.7E-05	4.2E-04
2 materials	2.39E-06	3.33E-05	2.3E-06	4.0E-05

proach described in Sub-section 2.3. Table 5 defines the four linear sections of the temperature dependency to be constructed; it also shows the temperature limits and BCs used to construct each of the four linear sections. Parameters a and b refer to the definition of each linear section as shown in Eq. 13 and Figure 1.

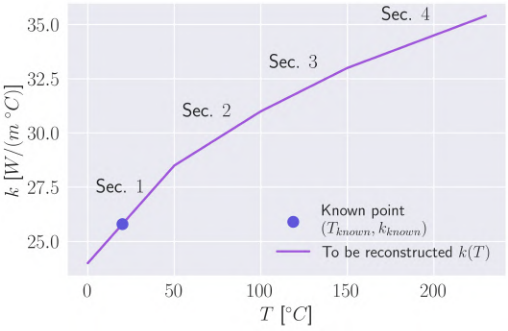

Figure 15: Piecewise linear thermal conductivity consisting of four sections and with T_{known} and k_{known} equal to 20.0°C and 25.8 $W/(m°\mathrm{C})$, respectively. Source: By authors.

Table 6 presents the results. It demonstrates that the nonlinear thermal conductivity and the corresponding solutions are successfully constructed for a specific measurement location numbers. The table reports the relative errors between the reconstructed and reference conductivities k, presenting both the average and maximum values across the four linear segments. In addition, it provides the relative errors between the constructed and reference temperature fields. This table also summarises the corresponding average and maximum values for the four linear sections (Figure 15).

Table 5: Four linear segments of the temperature dependence, along with their corresponding temperature limits and BCs used for constructing each segment (Figure 15). Source: By authors.

Section	a **[$W/m°C^2$]**	b **[$W/m°C$]**	**Limit 1**	**Limit 2**	v_c **[m/s]**	q **[W/m^2]**
1	0.09	24.0	$T_{r1} = 0°C$	$T_{r2} = 50°C$	1.0	33000
2	0.05	26.0	$T_{r2} = 50°C$	$T_{r3} = 100°C$	2.0	130000
3	0.04	27.0	$T_{r3} = 100°C$	$T_{r4} = 150°C$	2.0	240000
4	0.03	28.5	$T_{r4} = 150°C$	$T_{r5} = 230°C$	2.0	422000

Table 6: The results for nonlinear thermal conductivity construction (Figure 15). Source: By authors.

		k **relative errors**		$\{T\}$ **relative errors**	
No. of measurement locations	**Noise level σ** [%]	Avg. k error [%]	Max. k error [%]	Avg. $\{T\}$ error [%]	Max. $\{T\}$ error [%]
4	0.0	0.006	0.016	0.0001	0.0002
4	0.2	55.514	129.697	12.109	28.021
4	1.0	16.537	27.119	15.837	181.358
4	$\sigma(T)$	55.514	129.697	15.511	28.672
8	0.0	4.829e-05	9.568e-05	1.29e-06	9.92e-06
8	0.2	5.252	7.964	0.51	1.122
8	1.0	16.537	27.119	4.027	16.329
8	$\sigma(T)$	6.241	9.474	0.953	2.986
11	0.0	3.751e-05	1.458e-04	3.5e-07	9.73e-06
11	0.2	3.976	12.241	0.107	1.04
11	1.0	14.822	24.45	1.796	4.375
11	$\sigma(T)$	8.807	22.251	2.237	34.25
17	0.0	6.8e-06	2.177e-05	3.4e-07	6.14e-06
17	0.2	3.646	6.545	0.195	2.614
17	1.0	6.348	9.474	1.067	8.411
17	$\sigma(T)$	6.063	9.444	0.839	3.289

As anticipated, for a fixed number of measurement locations, the relative construction errors tend to rise with increasing noise levels. This behaviour is further illustrated in Figure 16, which shows the time evolution of the relative thermal conductivity errors. A similar trend is observed in the stand-alone solution construction discussed earlier in Sub-section 3.2.

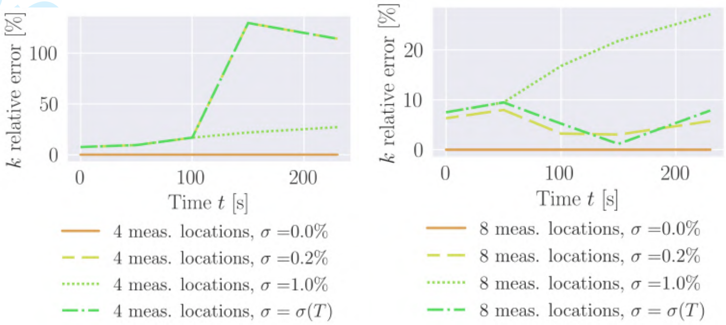

(a) 4 measurement locations (b) 8 measurement locations

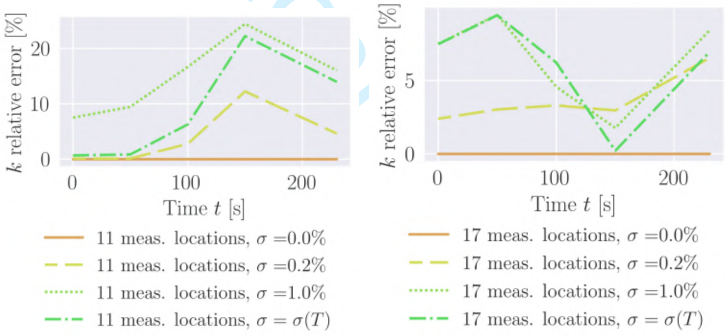

(c) 11 measurement locations (d) 17 measurement locations

Figure 16: The progress of relative thermal conductivity error with time for various measurement locations (Figure 4). Source: By authors.

All noise-free cases yield great accuracy, displaying errors on the order of 10^{-3} or lower. However, the performance declines sharply for some measurement configurations when noise is introduced. In particular, cases with only 4 measurement locations struggle to handle even 0.2% noise, often resulting in errors exceeding 100%, which renders the constructed thermal conductivity and temperature fields unreliable. In contrast, increasing the number of measurement locations leads to a marked improvement in reconstruction performance. The best results are obtained with 17 measurement points, where errors remain below 10% across all examined noise levels. These findings are further corroborated by the spatial distributions of the relative $\{\boldsymbol{T}\}$ errors shown in Figure 17. They exhibit similar patterns to those discussed in Section 3.2 (Figures 9 and 10). Specifically, increasing the number of measurement locations leads to a reduction in the average relative $\{\boldsymbol{T}\}$ errors, while the maximum errors become concentrated near the corners of the upper surface of the tile.

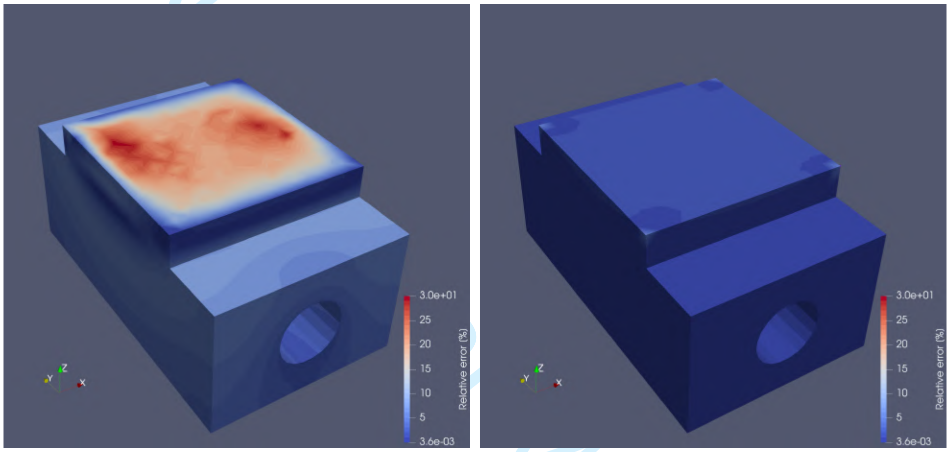

(a) 4 measurement locations (b) 17 measurement locations

Figure 17: The spatial distribution of relative $\{\boldsymbol{T}\}$ error for 4 and 17 measurement locations (Figure 4) for the thermocouple-specific noise level. Source: By authors.

4. Conclusions

In conclusion, this paper introduces a FE-based inverse analysis framework, which is combined with a modification of ODIL. Its potential is highlighted by analysing its application to the 3D heat conduction in an AMAZE sample, which was previously used in the fusion energy experiential facility.

The presented results demonstrate the effectiveness of the proposed approach for reconstructing the transient temperature field and thermal conductivity distributions within the sample using limited and potentially noisy temperature measurements. The transient solution construction successfully reproduces the full temperature field with reasonable accuracy, even when the number of measurement locations is restricted. The analysis reveals that measurement noise has a significant influence on reconstruction quality, as noise levels increase, both the average and maximum relative errors rise. The relatively large construction time step further amplifies these initial discrepancies, though the errors diminish as the system approaches steady-state conditions.

Increasing the number of measurement locations consistently improves reconstruction accuracy. While the average relative errors decrease with additional measurements, the spatial error distributions indicate that these improvements are not uniform across the domain. Regions near the top surface of the tile, especially the corners, tend to exhibit localised areas of higher error, even when the overall average accuracy improves. These findings suggest that while adding more sensors enhances global accuracy, strategic sensor placement remains critical for minimising localised reconstruction errors.

The reconstructed temperature fields also enable accurate estimation of the applied heat flux, with the evolution of the reconstructed heat flux closely matching the reference data after the initial transient phase. Both the average and maximum relative heat flux errors decrease as the number of measurement locations increases, further confirming the benefits of denser measurement configurations, particularly under noisy conditions.

For the thermal conductivity reconstruction, both linear and nonlinear cases demonstrate the robustness of the proposed framework. The method achieves highly accurate results under noise-free conditions, with errors on the order of 10^{-3} or lower. However, the presence of measurement noise can severely degrade performance when too few measurement points are available. Configurations with only four sensors fail to maintain reliability even at low noise levels, producing errors exceeding 100%. In contrast, using a larger number of measurement locations significantly improves reconstruction stability and accuracy. The best performance is observed with 17 measurement points, where errors remain below 10% across all tested noise levels.

Overall, the results confirm that the developed solution and material reconstruction framework is capable of accurately estimating transient thermal behaviour and temperature-dependent thermal properties. Its performance depends strongly on both the number and spatial distribution of measurement points, as well as the noise level in the input data. With an adequate number of measurements and moderate noise levels, the method demonstrates reliable reconstruction capability.

Finally, this approach utilises the traditional industry-standard simulation method for solid materials, which significantly simplifies the process of its integration into the existing simulation workflows in the industry. Piecewise linear material property representation are consistent with how material properties are typically represented in various simulation software. Thus, the results suggest significant potential for the DT applications.

5. Acknowledgements

This work has been part funded by the EPSRC Energy Programme [grant number EP/W006839/1]. The authors acknowledge the support of Supercomputing Wales and AccelerateAI projects, which is part-funded by the European Regional Development Fund (ERDF) via the Welsh Government. Furthermore, the authors gratefully acknowledge NVIDIA Academic Grant Program Award for supporting this research through the NVIDIA RTX 6000 Ada GPU grant. The completion of this paper would not have been possible without this valuable support.

References

[1] J.-F. Yao, Y. Yang, X.-C. Wang, X.-P. Zhang, Systematic review of digital twin technology and applications, Visual Computing for Industry, Biomedicine, and Art 6 (2023) 10. doi:10.1186/s42492-023-00137-4.

[2] A. Tarantola, Inverse Problem Theory and Methods for Model Parameter Estimation, Society for Industrial and Applied Mathematics, 2004.

[3] S. Arridge, P. Maass, O. Öktem, C.-B. Schönlieb, Solving inverse problems using data-driven models, Acta Numerica 28 (2019) 1–174. doi:10.1017/S0962492919000059.

[4] A. Bangian-Tabrizi, Y. Jaluria, An optimization strategy for the inverse solution of a convection heat transfer problem, International Journal of Heat and Mass Transfer 124 (2018) 1147 – 1155. doi:10.1016/j.ijheatmasstransfer.2018.04.053.

[5] H. R. Tamaddon-Jahromi, N. K. Chakshu, I. Sazonov, L. M. Evans, H. Thomas, P. Nithiarasu, Data-driven inverse modelling through neural network (deep learning) and computational heat transfer, Computer Methods in Applied Mechanics and Engineering 369 (2020) 113217. doi:https://doi.org/10.1016/j.cma.2020.113217.

[6] H. Tercan, T. Meisen, Machine learning and deep learning based predictive quality in manufacturing: a systematic review, Journal of Intelligent Manufacturing 33 (2022) 1879–1905. doi:10.1007/s10845-022-01963-8.

[7] S. Le Clainche, E. Ferrer, S. Gibson, E. Cross, A. Parente, R. Vinuesa, Improving aircraft performance using machine learning: A review, Aerospace Science and Technology 138 (2023) 108354. doi:https://doi.org/10.1016/j.ast.2023.108354.

[8] I. Goodfellow, Y. Bengio, A. Courville, Deep Learning, The MIT Press, 2016.

[9] C. Rasmussen, C. Williams, Gaussian Processes for Machine Learning, Adaptive Computation and Machine Learning series, MIT Press, 2005.

[10] B. Mehlig, Machine Learning with Neural Networks: An Introduction for Scientists and Engineers, Cambridge University Press, 2021. doi:10.1017/9781108860604.

[11] G. Yagawa, H. Okuda, Neural networks in computational mechanics, Archives of Computational Methods in Engineering 3 (1996) 435 – 512. doi:10.1007/BF02818935.

[12] W. Bielajewa, M. Tindall, P. Nithiarasu, Comparative study of transformer- and lstm-based machine learning methods for transient thermal field reconstruction, Computational Thermal Sciences: An International Journal 16 (2024). doi:10.1615/ComputThermalScien.2023049936.

[13] R. Lewis, Simulation driven machine learning methods to optimise design of physical experiments and enhance data analysis for testing of fusion energy heat exchanger components, Phd thesis, Swansea University, 2023.

[14] Y. Zhang, Z. Gong, W. Zhou, X. Zhao, X. Zheng, W. Yao, Multi-fidelity surrogate modeling for temperature field prediction using deep convolution neural network, Engineering Applications of Artificial Intelligence 123 (2023) 106354. doi:https://doi.org/10.1016/j.engappai.2023.106354.

[15] F. Zhu, J. Chen, D. Ren, Y. Han, Transient temperature fields of the tank vehicle with various parameters using deep learning method, Applied Thermal Engineering 230 (2023) 120697. doi:https://doi.org/10.1016/j.applthermaleng.2023.120697.

[16] A. Di Meglio, N. Massarotti, P. Nithiarasu, A physics-driven and machine learning-based digital twinning approach to transient thermal systems, International Journal of Numerical Methods for Heat & Fluid Flow 34 (2024) 2229–2256. URL: `https://doi.org/10.1108/HFF-10-2023-0616`. doi:10.1108/HFF-10-2023-0616.

[17] A. D. Meglio, N. Massarotti, P. Nithiarasu, Digital twins of thermal systems: a comparison between supervised and reinforcement learning, Computational Thermal Sciences: An International Journal 17 (2025) 39–46. doi:10.1615/ComputThermalScien.2025057435.

[18] M. Raissi, P. Perdikaris, G. E. Karniadakis, Physics-informed neural networks: A deep learning framework for solving forward and inverse problems involving nonlinear partial differential equations, Journal of Computational Physics 378 (2019) 686–707. doi:https://doi.org/10.1016/j.jcp.2018.10.045.

[19] P. Sharma, L. Evans, M. Tindall, P. Nithiarasu, Stiff-pdes and physics-informed neural networks, Archives of Computational Methods in Engineering 30 (2023) 2929–2958. doi:10.1007/s11831-023-09890-4.

[20] P. Karnakov, S. Litvinov, P. Koumoutsakos, Flow reconstruction by multiresolution optimization of a discrete loss with automatic differentiation, The European Physical Journal E 46 (2023) 59. doi:10.1140/epje/s10189-023-00313-7.

[21] P. Karnakov, S. Litvinov, P. Koumoutsakos, Solving inverse problems in physics by optimizing a discrete loss: Fast and accurate learning without neural networks, PNAS Nexus 3 (2024) pgae005. doi:10.1093/pnasnexus/pgae005.

[22] D. Hancock, Employing Additive Manufacturing for Fusion High Heat Flux Structures, Phd thesis, University of Sheffield, 2018.

[23] R. Lewis, Simulation driven machine learning methods to optimise design of physical experiments and enhance data analysis for testing of fusion energy heat exchanger components, Phd thesis, Swansea University, 2023.

[24] Å. Björck, Numerical Methods for Least Squares Problems, Society for Industrial and Applied Mathematics, 1996. doi:10.1137/1.9781611971484.

[25] S. Gratton, A. S. Lawless, N. K. Nichols, Approximate gauss–newton methods for nonlinear least squares problems, SIAM Journal on Optimization 18 (2007) 106–132. doi:10.1137/050624935.

[26] ANSYS, Inc., Ansys software, Available at `https://www.ansys.com/`, 2023. [Software].

[27] R. Cimrman, V. Lukeš, E. Rohan, Multiscale finite element calculations in python using sfepy, Advances in Computational Mathematics (2019). doi:10.1007/s10444-019-09666-0.

[28] T. D. Marshall, D. L. Youchison, L. C. Cadwallader, Modeling the nukiyama curve for water-cooled fusion divertor channels, Fusion Technol. 35 (2001) 8–16. URL: `http://film2000.free.fr/TOFE.pdf`.

[29] F. Seibold, P. Ligrani, B. Weigand, Flow and heat transfer in swirl tubes — a review, International Journal of Heat and Mass Transfer 187 (2022) 122455. doi:https://doi.org/10.1016/j.ijheatmasstransfer.2021.122455.

[30] M. Araki, M. Ogawa, T. Kunugi, K. Satoh, S. Suzuki, Experiments on heat transfer of smooth and swirl tubes under one-sided heating conditions, International Journal of Heat and Mass Transfer 39 (1996) 3045–3055. doi:https://doi.org/10.1016/0017-9310(95)00344-4.

[31] R. M. Park (Ed.), Manual on the Use of Thermocouples in Temperature Measurement, 4th ed., ASTM Committee E20, 1993.